Modeling, Magnetic Design, Simulation Methods, and Experimental Evaluation of Various Powder Cores Used in Power Converters Considering Their DC Superimposition Characteristics

Jun Imaoka, *Member, IEEE*, Kenkichiro Okamoto, Masahito Shoyama, *Senior Member, IEEE*, Yuki Ishikura, Mostafa Noah, *Student Member, IEEE*, and Masayoshi Yamamoto, *Member, IEEE*

***Abstract*—Powder cores have been gaining much attention as one of the attractive magnetic cores used in power converters due to their superior features such as high saturation flux density and their capability to suppress fringing flux due to the distributed airgaps. However, powder cores have a unique feature that the relative permeability of the magnetic core varies depending on the magnetic field intensity. The comprehensive modeling of variable relative permeability, design method of powder cores, and computer simulation methods are not well discussed in the relevant literature. This paper proposes a novel modeling, magnetic design method, and simulation technique considering dc superimposition characteristics of powder cores. The modeling method relies on a simple novel model equation representing the behavior of the variable relative permeability under the dc current superimposition condition, which is helpful to evaluate the performance of powder cores and to properly design various magnetic components. In this evaluation, five different magnetic powder cores are used to show the accuracy and properness of the proposed method. Theoretical analysis has been presented and the effectiveness of the proposed methods has been evaluated through simulation and experimental tests.**

***Index Terms*—Circuit simulation, dc–dc converter, dc superimposition characteristic, magnetic circuits, magnetic cores, nonlinear inductance, permeability measurement, powder cores.**

Manuscript received July 17, 2018; revised October 18, 2018; accepted November 26, 2018. Date of publication December 10, 2018; date of current version June 10, 2019. This work was supported in part by the Japan Society for the Promotion of Science KAKENHI Grant JP16K18059. Recommended for publication by Associate Editor Dr. B. Chen. *(Corresponding author: Jun Imaoka.)*

J. Imaoka, Y. Ishikura, and M. Noah are with the Department of Electrical Engineering, Nagoya University, Nagoya 464-8601, Japan (e-mail:

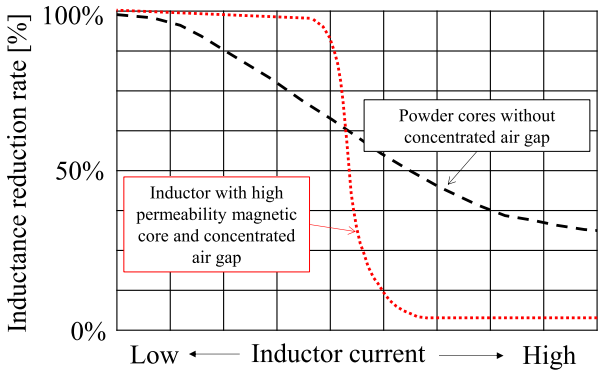

Fig. 1. Inductance variation caused by increasing inductor current.

[9]–[13]. Therefore, ferrite cores may be unsuitable for high-temperature environments. On the other hand, powder cores usually consist of Fe-based magnetic powders, which have high Curie temperature property. Although the Curie temperature of powder core differs depending on alloy composition, Curie temperature is usually in the range of 400–700 °C [14]–[17].

3) High flexibility of the magnetic structure: Powder cores are processed by applying pressure molding using a mold. If a mold had been prepared, powder cores can be formed into various shapes. From a magnetic structural perspective, low profile or planar magnetic shape is effective for reducing temperature rise because thermal resistance can be reduced by increasing the surface area of magnetic components [18], [19]. Therefore, the high flexibility of the magnetic core shape is one of the attractive features.
4) Soft-saturation property: Soft-saturation means that the inductance value gradually drops as the inductor current value increases. The powder cores have this property. The inductance variation caused by increasing inductor current is shown in Fig. 1. In general, in an inductor with high permeability magnetic core and concentrated airgaps, the inductance value drops rapidly when the maximum flux density exceeds the core saturation limit, which is determined by the core material. The soft saturation property of the powder core can be considered as an attractive feature because it has a better reliability while encountering a sudden overcurrent.
5) Eliminating the fringing flux: High permeability magnetic cores such as Mn-Zn ferrite cores require inserting concentrated airgaps to the core when dc current flows through the winding. Although magnetic saturation can be avoided by inserting the airgap as shown in Fig. 2(a), the concentrated airgap produces fringing flux, which is one of the causes of high-frequency core and winding losses near the concentrated airgaps. For example, in case of nanocrystalline ribbon cores with a concentrated airgap, the eddy current loss on the core surface produced by the fringing flux dramatically increase as reported in [20], [21]. In [22]–[24], the fringing loss is restrained by edging the corner of the core at airgap or by distributing a concentrated airgap into several airgaps because the expansion range of the fringing flux can be suppressed. However, this process increases the production cost. Conversely, powder cores are manufactured from very fine particles of magnetic materials and they do not require inserting concentrated airgaps in general.

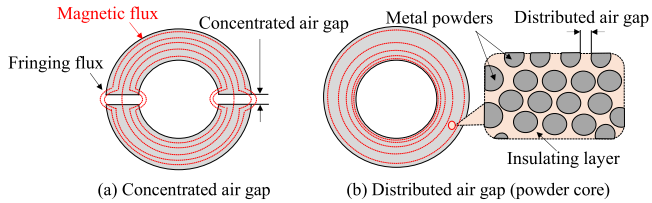

Fig. 2. Magnetic core with concentrated or distributed airgaps. (a) Concentrated airgap. (b) Distributed airgap (powder core).

B. Non-Linear Properties of Powder Cores

Although powder cores have many attractive magnetic properties, the relative permeability of the core is usually very low (initial permeability $\mu_r < 200$) compared with other magnetic materials such as Mn-Zn ferrite cores, because of the distributed airgaps between metal powders in cores. In addition, powder core has dc superposition characteristics in which the inductance value changes non-linearly depending on the instantaneous current value. The reason why the inductance value changes non-linearly according to the dc current value can be interpreted as follows: For example, in a toroidal metal powder structure shown in Fig. 2(b), magnetic flux density on the inner magnetic path of the toroidal core shape becomes higher than that on the outer magnetic path. The reason is that the magnetic reluctance in the inner magnetic path is lower than that in the outer magnetic path because the inner magnetic path length is shorter than the outer one. Therefore, the magnetic flux generated from the magnetomotive force easily flows into the inner side of the toroidal core and magnetic saturation occurs from the inner magnetic path. Thus, powder cores with low-permeability property have the magnetic structural dependency on dc superposition characteristics. As a matter of fact, the structure of the insulating layer between the powders shown in Fig. 2(b) also affects the dc superposition characteristic [25], [26].

In terms of the designing magnetic components, inductor ripple currents should be designed considering inductance variation with increasing dc current values. Designing an inductor considering the maximum value of ripple current at heavy load is one of the most important parts in the design process because it affects the power losses and temperature rise in power semiconductor devices and other passive components. Furthermore, since the relative permeability of powder cores changes depending on the magnetic field intensity, the dc superposition characteristic of the powder core affects the number of turns to obtain the required inductance value.

C. Literature Review of Modeling Methods of Non-Linear Relative Permeability for Designing Inductor

In order to design an inductor considering the dc superposition characteristic, modeling techniques including non-linear

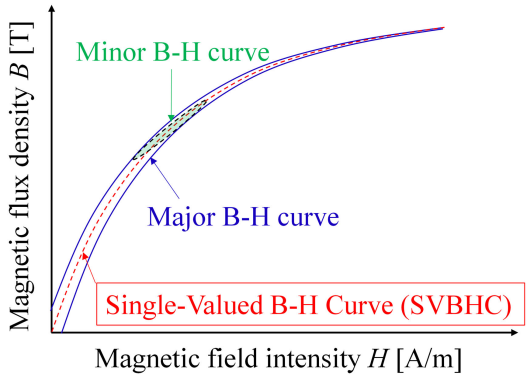

Fig. 3. Meaning of SVBHC.

relative permeability are important to be considered and they have been previously discussed. For instance, in order to simulate a magnetic component, the Preisach, Jiles–Atherton, Stoner–Wohlfarth models are well known as physics-based macroscopic models of hysteresis [27]. In addition, the modeling method based on the Preisach model and the permeance-based circuit theory was proposed for simulating magnetic devices in power converter systems [28]. These modeling methods can implement non-linear magnetic properties into circuit simulators and can achieve good accuracy for simulating magnetic components and may be suitable for system-level evaluation.

From the magnetic components design perspective, various inductor design methods considering non-linear relative permeability or non-linear inductance had been reported in [29]–[41]. For designing inductor used in power converter applications, a non-linear relative permeability measured from the single-valued B-H curve (SVBHC) shown in Fig. 3 is often used. SVBHC means the centerline of the major B-H loop and minor B-H Loop [29]. By using non-linear relative permeability measured from SVBHC or non-linear inductance, the ripple current in dc–dc converter under discontinue current mode (DCM) and continues current mode (CCM) conditions can be estimated approximately, as presented in [29]–[31]. As another application of using SVBHC, an inductor design method using cores with different permeability has been proposed in [32] and [33]. A proposal of coupled multilayer chip inductors has been presented in [34], and high power density inductor used for point of load applications has been proposed in [35]–[38]. In the literature, non-linear permeability measured from SVBHC is modeled relying on measured experimental data or data sheets. In order to propose simple design methods of non-linear magnetic components and implement non-linear characteristics into circuit simulator, establishing a mathematical modeling method is important. Li *et al.* [36], [39]–[41] proposed a mathematical fitting function using coefficients, which shows the dependency of non-linear relative permeability on magnetic field intensity. However, these coefficients used in the modeling equations are used for fitting experimental parameters only. Therefore, magnetic material properties cannot be intuitively understood from the coefficients. Therefore, this paper proposes new modeling equations representing non-linear relative permeability. Establishing simple modeling techniques to extract the magnetic material properties is essential to accurately model the behavior of various magnetic devices operated in circuit simulators and expanding of design approaches for magnetic components. Furthermore, simple coefficients used in model equations are helpful to simplify the communication between circuit or magnetic device designers and material developers.

In fact, power semiconductor device models operate on LT Spice, PLECS are available online in recent years [42]–[44] and circuit designer can use power semiconductor device models. By expanding this idea to passive components, there is a further possibility that designing the power converter can be very easy by connecting with artificial intelligence, which has a function of selecting optimal devices from big data related to components on the internet. Therefore, modeling passive components is significantly important for the future. Therefore, this paper proposes modeling and design methods focusing on the non-linear relative permeability of powder cores. Experimental tests had been conducted to evaluate the proposed model.

D. Contents of This Paper

As mentioned above, this paper proposes comprehensive analysis considering the non-linearity of relative permeability modeling of powder core materials. Furthermore, the proposed modeling and magnetic design method rely on a simple mathematical function, considering dc superimposition characteristics for powder cores used in power converters. The contributions and contents of this paper are as follows.

1) A novel mathematical function representing the non-linear relative permeability is proposed. As an attractive feature of the proposed mathematical function, this function has only three coefficients, and each coefficient can be understood intuitively. In addition, these coefficients are automatically parameterized by using experimental data and computer calculation.
2) Various powder core inductors had been constructed from different alloy composition and are compared to evaluate magnetic properties related to relative permeability under dc current superimposed condition. This evaluation is helpful for selecting magnetic materials as one of the references.
3) A magnetic design method considering dc-superimposition characteristics is introduced using a proposed model equation representing the non-linear relative permeability. By utilizing the numerical calculation, a desired inductance can be easily designed considering dc current superimposition and square wave voltage magnetizing condition. In addition, the estimation method of magnetic flux density is also proposed.
4) A simulation model using a multi-domain circuit simulator is introduced. The simulator can conduct a coupled analysis of magnetic and electrical circuits. Simulation waveforms and experimental waveforms are compared side by side to evaluate the proposed magnetic device model. The simulation waveforms are highly consistent with experimental waveforms. Therefore, the proposed model has been proven effective.

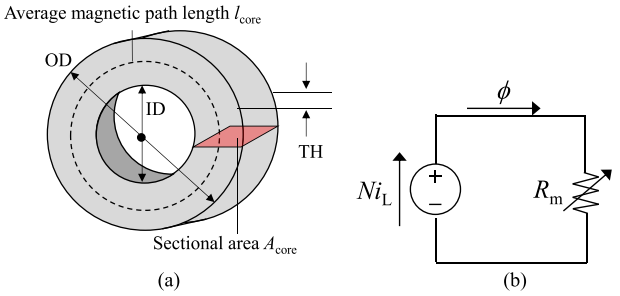

Fig. 4. Toroidal magnetic core. (a) Magnetic structure. (b) Magnetic circuit model.

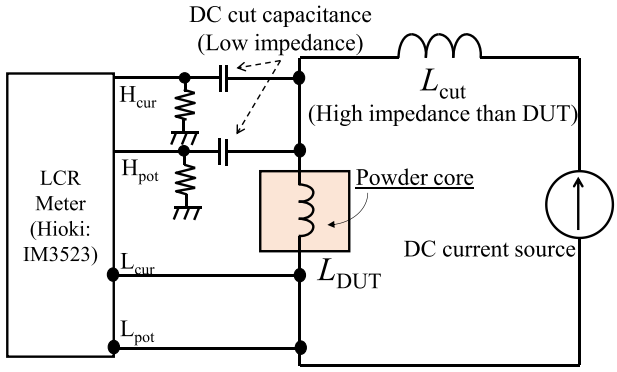

Fig. 5. Measurement system for relative permeability of powder core under dc superimposition condition.

This paper is an extended discussion of [45]. The new contents include developing the literature review, important points for measuring non-linear relative permeability, proposing a calculation method of ripple current using numerical analysis based on piecewise linear calculation, and additional experimental results are added to show the effectiveness of the theoretical discussion.

This paper is divided into six sections. Section II discusses the model equation, which shows that the relative permeability is dependent on magnetic field intensity. A newly developed equation with only three coefficients is proposed. The three coefficients can be extracted from experimental tests. The meaning of the proposed model equation and the three coefficients are described in Section II. In Section III, by using the proposed model equation, a magnetic design method of an inductor using a powder core to obtain the desired inductance value is also proposed. Furthermore, an implementation method for the model equation into a circuit simulator is also proposed in Section IV. In Section V, the proposed magnetic design method is validated by conducting experimental tests. Furthermore, the experimental waveforms are side by side compared with simulation waveforms. Finally, conclusions are presented in Section VI.

II. Modeling of Relative Permeability Depending on Magnetic Field Intensity

A. Experimental Measurement Method for Non-Linear Relative Permeability of Powder Cores

First, a measurement method for non-linear relative permeability is introduced in this section. The magnetic core structure and magnetic circuit model of an inductor are shown in Fig. 4. where Ni_L is the magnetomotive force expressed by the product of the number of turns N and the inductor current i_L. $l_{\rm core}$ is the average magnetic path length, $A_{\rm core}$ is the sectional area of the core. R_m means the magnetic reluctance of the closed magnetic path of the toroidal core. It is worth mentioning that the core reluctance is a variable parameter depending on the value of winding current. From this magnetic circuit model, the inductance $L_{\rm self}$ can be expressed as

$$L_{\rm self} = \frac{N^2}{R_m} = N^2 \cdot P_m = \left(\frac{N^2 \cdot \mu_0 \cdot \mu_r \cdot A_{\rm core}}{l_{\rm core}}\right) \quad (1)$$

where μ_0 is the space permeability, and it equals $4\pi \times 10^{-7}$ H/m. P_m means the permeance of the core. Besides, the inductance $L_{\rm self}$ varies as the function of the inductor current i_L. It can be deduced from (1) that the variable parameter, which has the dependency on the inductor current, is the relative permeability because N, μ_0, $A_{\rm core}$, and $l_{\rm core}$ are constant parameters, at a fixed inductance value. Therefore, in order to design an inductor considering dc superimposition characteristic, a precise modeling of relative permeability under dc excitations condition is necessary.

Fig. 5 shows a measurement system for the relative permeability of powder cores under dc superimposition condition [46]. This system consists of *LCR* meter (HIOKI, model number: IM3523), two resistors, and two capacitors to block the dc component, and two capacitors have low impedance at the measured frequency. These resistors and capacitors are utilized to protect the *LCR* meter. The ripple cut inductor $L_{\rm cut}$ has a large inductance value to minimize the ac components, and it is connected in series with the dc current source to prevent flowing out of the small signal of the *LCR* meter to the dc current source side. In order to measure the relative permeability of powder cores, first of all, an optional number of turns is wounded to a powder core $L_{\rm DUT}$ [device under test (DUT)]. Under this condition, inductance value $L_{\rm DUT}$ is measured while changing dc current value of the dc current source. Then, by using (1), the relative permeability of the cores can be calculated from measured inductance values. However, when selecting a low value of $L_{\rm cut}$, the measured value of $L_{\rm DUT}$ may include an error. If an accurate value of $L_{\rm cut}$ is comprehended in advance, a better accuracy of $L_{\rm DUT}$ can be calculated by $L_{\rm DUT} = (L_{\rm cut} \cdot L_{\rm measured})/(L_{\rm cut} - L_{\rm measured})$, where $L_{\rm measured}$ are measured inductance value of *LCR* meters.

While measuring the relative permeability, an optimal number of turns can be selected considering the following.

1) The influence of the parasitic capacitance between the winding of DUT.
2) The magnetic field intensity level that is required to be measured.

In the DUT with a large number of turns: In order to measure the relative permeability up to the high magnetic field intensity level with low dc current, the large number of turns are effective. However, the parasitic capacitance between windings of DUT would increase. The parasitic capacitance [known as equivalent parallel capacitance (EPC)] negatively affects the

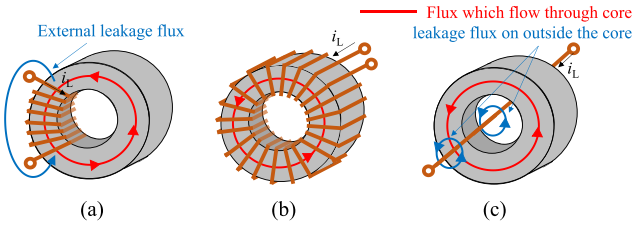

Fig. 6. Winding arrangement of DUT for measuring relative permeability. (a) Uneven winding. (b) Uniform winding. (c) Single turn.

measurement obtained from the *LCR* meter. This is because the measured inductance value of *LCR* meter is a converted value from the magnitude of impedance (|Z|), phase (θ), and specified circuit models (for example, series *L* and series resistance *R*). If the measured frequency reached the parallel resonant frequency [known as self-resonant frequency (SRF)] decided by $L_{\rm self}$ and EPC of DUT, the inductance value cannot be measured accurately. Therefore, the measured frequency should be set at a lower frequency with a margin from SRF. One more thing shall be considered is the winding arrangement of DUT. In case of the uneven winding are wounded to DUT, as shown in Fig. 6(a), the leakage flux flows not only through the core, but also through the external side of the core. Therefore, in order to accurately measure inductance value, the optional winding shall be uniformly wounded as shown in Fig. 6(b).

In the DUT with a low number of turns: if lower winding turns are selected, although the effect of parasitic capacitance can be reduced, dc current source, which can deliver high current is needed to produce high magnetic field intently level that needed to be measured. It is worth mentioning that a single turn may be not suitable for an accurate measurement because the leakage flux may flow through space outside of DUT as shown in Fig. 6(c). This leakage flux affects the accurate measurement. By considering the above conditions, an optimal number of turns is selected, as discussed in Section II-C.

B. Conventional Model Equations and Proposed Model Equation Representing Relative Permeability

Relative permeability of powder cores can be measured by applying the above procedure. However, such many measurement data obtained from the experiments are difficult to process mathematically in designing magnetic components or in implementing dc superimposition characteristics to a circuit simulator.

A review of the model equations showing the relative permeability obtained from the measured relative permeability is conducted. From the related literature, some modeling equations have been proposed. For instance, Brauer's model was proposed in 1975 [40], [41]. In addition, the generalized model of the non-linear relative permeability to adapt the positive and negative value of flux density *B* is proposed and is shown by the following equation [41]:

$$\mu_r(B) = \frac{1}{k_1 \cdot (1 + 2k_2 B^2)\, e^{k_2 B^2} + k_3} \tag{2}$$

where k_1, k_2, and k_3 are the Brauer's model constants for each magnetic material and these constant parameters is obtained by fitting the measured B-H curves. As another model, the following equation is proposed in [36] to show the relationship between flux density and magnetic field intensity, and a similar equation proposed in [39]

$$B(H) = 0.1 \cdot \left(\frac{a + b \cdot H + c \cdot H^2}{1 + d \cdot H + e \cdot H^2} \right)^x \tag{3}$$

where *a*, *b*, *c*, *d*, *e*, and *x* are the constant parameters to fit the measured B-H curve data. *H* is the magnetic field intensity and given by

$$H = \frac{N \cdot i_L}{l_{\rm core}}. \tag{4}$$

These equations shown in (2) and (3) have many coefficients for fitting measured SVBHC curves. Furthermore, these coefficients do not have any physical meanings. Therefore, non-linear magnetic permeability cannot be understood intuitively from these coefficients.

In order to simplify the model equation and coefficients, this paper proposes a novel model equation and is shown by

$$\mu_r(H) = 1 + \frac{p}{1 + (|H|/q)^r} \tag{5}$$

where *p*, *q*, and *r* are the coefficients representing the relationship between the inductor current and the relative permeability.

For the intuitive interpretation of the proposed model equation, the conceptual diagram using (5) is illustrated in Fig. 7(a). As seen in Fig. 7(a), *p* is a parameter related to initial relative permeability at zero dc current condition. In addition, the initial relative permeability is shown by $p + 1$. *q* means the magnetic field intensity where the initial relative permeability reaches its half value. The first term on right-hand side in (5) means the relative permeability of the core when complete magnetic saturation occurs. Therefore, (5) converges to 1 if *H* becomes infinite, as shown in Fig. 7(b). *r* is the coefficient related to the negative slope of the relative permeability. The variation of relative permeability when the coefficients *r* change is shown in Fig. 7(c). As seen in Fig. 7(c), when *r* has a high value, the relative permeability tends to rapidly decrease at around the *q*. In addition, the slope of the relative permeability at *q* can be expressed as $-pr/4q$. Therefore, the model equation shown in (5) is helpful because the meaning of each coefficient can be intuitively understood. Furthermore, these coefficients are helpful to evaluate dc superimposition characteristics of various magnetic materials. The proposed equation is derived on the basis of the Fermi–Dirac distribution function because the function is similar to the change behavior of relative permeability of powder cores.

C. Evaluating the Proposed Model Equation for Various Powder Cores With Different Magnetic Properties

The experimental tests and mathematical analysis are conducted to validate whether the proposed model equation can actually accurately fit the measured values of relative permeability or not. Five different magnetic materials have been evaluated in this discussion. Table I shows the magnetic materials and their core size used in this evaluation, and the magnetic cores are

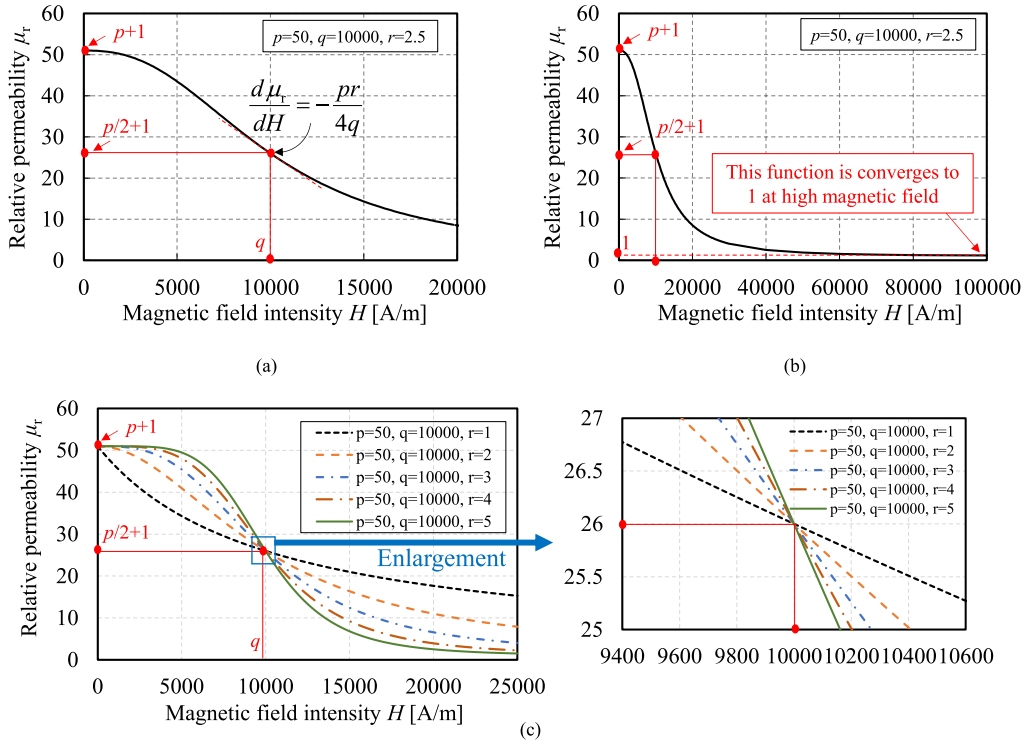

Fig. 7. Interpretation of proposed model equation showing relative permeability that depends on magnetic field intensity. (a) Coefficients expressing relative permeability. (b) Proposed model equation at higher values of magnetic field intensity. (c) Behavior of relative permeability when the coefficients r varies.

TABLE I
MAGNETIC MATERIALS AND SIZE OF THE TOROIDAL CORES

Type	Magnetic material	Model number	Chemical component	Outer Diameter (OD)	Inner Diameter (ID)	Thickness (TH)	Sectional area A_{core}	Average magnetic path length l_{core}
A	Ferrosilicon powder	BCW155-08150	Fe-Si	27.3mm	14.5mm	11.2mm	71.6mm^2	65.7mm
B	Permalloy powder	BCH15-02800	Fe-Ni	27.2mm	14.6mm	11.6mm	73.0mm^2	65.7mm
C	Supermalloy powder	BCM15-02800	Ni-Fe-Mo	27.2mm	14.6mm	11.8mm	74.3mm^2	65.7mm
D	Sendust powder	BCS15-02750	Fe-Si-Al	27.4mm	14.3mm	11.7mm	76.6mm^2	65.5mm
E	Amorphous powder	GLT114D	Fe-P-C-B-Si	27.4mm	14.7mm	11.9mm	75.6mm^2	66.1mm

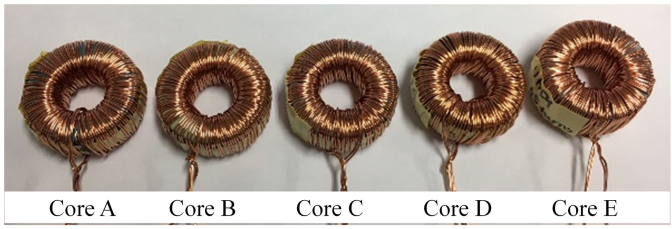

Fig. 8. Prototypes of the inductors using toroidal core shown in Table II. The number of turns in each core is 65 turns.

shown in Fig. 8. The magnetic cores have almost the same structure to guarantee a fair comparison and to eliminate any dependency of the relative permeability on the core dimensions, as mentioned in Section I.

The experimental conditions for this evaluation are as follows: the measured frequency is 50 kHz, the small signal voltage of *LCR* meter is 1 V. The number of turns in each DUT is 65 turns, and dc current range is from 0 to 18 A in order to change the dc magnetic field intensity. In addition, 65 turns are selected considering SRF. SRF is checked in advance whether it is much higher than the measured frequency (50 kHz) or not. The measured results of SRF in each core with 65 turns is shown in Fig. 19 in Appendix A and are over 1 MHz. The measured results of the relative permeability in each magnetic core are shown in Fig. 9(a) and (b). In Fig. 9(a), the dots mean the experimentally measured results, and the solid lines show the approximate lines obtained from the proposed model equation shown in (5). As seen in Fig. 9(a), the experimental results and the calculated results from our proposed equation (5) are consistent with each other. On the other hand, Fig. 9(b) shows the measured results and approximated lines using the least-squares method relying on a sixth-order polynomial expression ($\mu_r = k_1 H^6 + k_2 H^5 + k_3 H^4 + k_4 H^3 + k_5 H^2 + k_6 H + k_7$). In this case, a high-order polynomial expression is applied to measured results to fit them. In case of using polynomial expressions of first to fifth order, the error between the calculated and measured results was relatively high. As seen in Fig. 9(b), the approximation line using the polynomial expression of sixth order is actually fitting with measured results up to the measured result at the highest magnetic field intensity (almost $H = 18000$ A/m). However, as seen in Fig. 9(b), the relative permeability of the least-squares

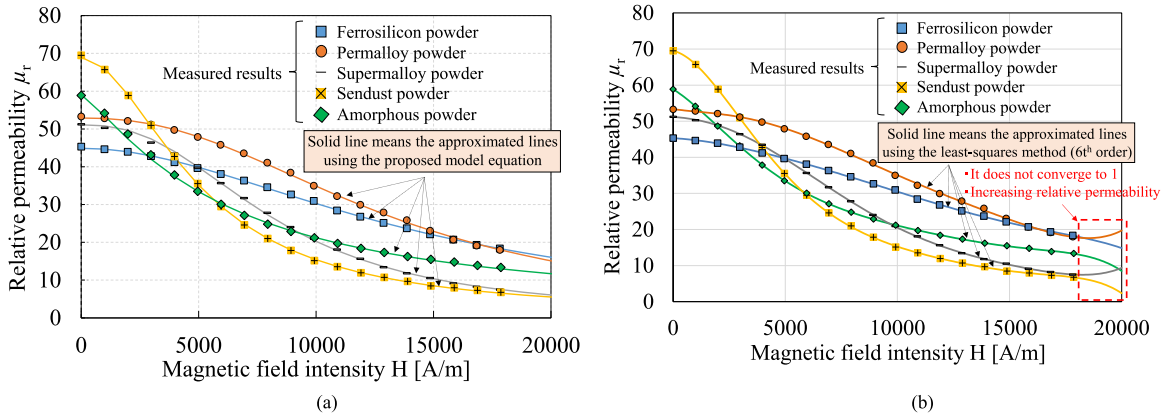

Fig. 9. Comparison results between the measured results and approximated lines using the proposed method and the least-squares methods. (a) Proposed model equation. (b) Least-squares method using sixth-order polynomial expression.

method using the polynomial expression does not converge to 1 at high magnetic field condition. In the case of the Permalloy (B) and the Supermalloy cores (C), the relative permeability using polynomial expression increase between $H = 18\,000$ A/m and 20 000 A/m. Therefore, if the polynomial expression is applied for making approximation line, many measured results at values of the high magnetic field are necessary to converge to 1.

As an extracting method of each coefficient in both methods, the coefficients showing relative permeability used in proposed model equations and the least-squares method using polynomial expression are automatically parametrized by using computer calculation. In this case, Mathematica (Wolfram Research) is used to calculate the coefficients.

The calculated coefficients p, q, and r in each core are summarized in Table II. In order to compare the coefficients between proposed and polynomial expressions, the coefficients of sixth-order polynomial expression are also shown in Table II. As seen in Table II, the meaning coefficients in the proposed model equation can be intuitively understood. Furthermore, the proposed equation has only three coefficients.

On the other hand, although the coefficients k_7 of the least-squares method using sixth-order polynomial expression means the initial relative permeability, the other parameters $k_1 \sim k_6$ cannot be intuitively understood.

Furthermore, the slope of $d\mu_r/dH$ at q in both methods is compared and the results are also shown in Table II. The values of the slope of $d\mu_r/dH$ at q are almost matched, and the calculated results of the proposed model equation are consistent with the measured results, with high accuracy. Therefore, the effectiveness of the proposed modeling method is confirmed. The validity of r values parametrized by computer calculation is verified in Appendix B.

III. Magnetic Design Method for Powder Cores

A. Calculating the Number of Turns

In this section, a design method of powder cores used in power converter is introduced by using the proposed model equation shown in (5). As a case study, the proposed magnetic design method is applied to an inductor used in a boost converter shown in Fig. 10(a).

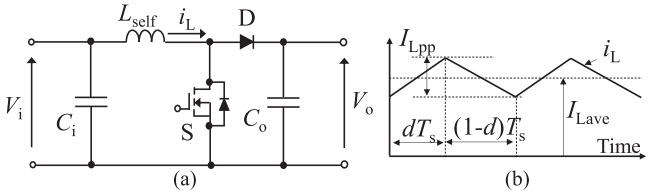

Fig. 10. Circuit diagram and current waveforms of the boost converter. (a) Circuit configuration. (b) Inductor current waveform.

Since the coefficients used in (5) are already measured by the experiments, they express the relative permeability of each powder core material. Therefore, these coefficients are used for the magnetic design considering dc superimposition characteristics. Using (1), (4), and (5), an expression for the self-inductance L_{self} can be obtained, as a function of the variable inductor current, as follows:

$$L_{self} = \left(\frac{N^2 \cdot \mu_0 \cdot A_{core}}{l_{core}}\right) \cdot \left(1 + \frac{p}{1 + (N \cdot i_L/q \cdot l_{core})^r}\right). \tag{6}$$

Therefore, once the designed inductance value is decided, the number of turns can be derived by substituting the geometrical parameters of the powder core and the coefficients related to relative permeability into (6). Nonetheless, (6) is difficult to be solved with respect to the number of turns N. In this case, a numerical analysis using computer calculation is used to decide the number of turns N. By conducting a numerical analysis, the designed number of turns can be automatically calculated. The circuit parameters for evaluating the proposed magnetic design method are listed in Table III. In general, the inductor ripple current is designed at a maximum power rating of converter because the power losses and temperature rise in active/passive components should be considered in advance. Since most of the high-power converters operating in CCM are often used, therefore, in this evaluation, the inductor is designed considering CCM operation.

TABLE II
COEFFICIENTS SHOWING THE RELATIVE PERMEABILITY

Proposed model equation ($\mu_r=1+p/(1+(\lvert H\rvert/q)^r)$)					
Type	p [-]	q [A/m]	r [-]	$d\mu_r/dH$ at q ($=-pr/4q$)	
Ferrosilicon powder (A)	43.9	14300	1.94	−1.5m/kA	
Permalloy powder (B)	51.9	13100	2.33	−2.3m/kA	
Supermalloy powder (C)	50.1	8260	2.47	−3.7m/kA	
Sendust powder (D)	68.0	5020	1.91	−6.5m/kA	
Amorphous powder (E)	58.1	6020	1.24	−3.0m/kA	
The least-squares method ($\mu_r=k_1H^6+k_2H^5+k_3H^4+k_4H^3+k_5H^2+k_6H+k_7$), k_1~k_7 are the coefficients. $d\mu_r/dH$ at q is calculated by $6k_1q^5+5k_2q^4+4k_3q^3+3k_4q^2+2k_5q+k_6$					
Type	k_1	k_2	k_3	k_4	k_5	k_6	k_7	$d\mu_r/dH$ at q in each core
Ferrosilicon powder (A)	$-5.160\cdot10^{-24}$	$2.804\cdot10^{-19}$	$-5.891\cdot10^{-15}$	$6.543\cdot10^{-11}$	$-4.552\cdot10^{-7}$	$-1.730\cdot10^{-4}$	44.9	−1.5 m/kA
Permalloy powder (B)	$8.986\cdot10^{-24}$	$-5.015\cdot10^{-19}$	$1.046\cdot10^{-14}$	$-9.018\cdot10^{-11}$	$1.326\cdot10^{-7}$	$-4.395\cdot10^{-4}$	53.0	−2.4 m/kA
Supermalloy powder (C)	$9.949\cdot10^{-24}$	$-5.341\cdot10^{-19}$	$9.507\cdot10^{-15}$	$-4.183\cdot10^{-11}$	$-3.767\cdot10^{-7}$	$-2.636\cdot10^{-4}$	51.1	−3.8 m/kA
Sendust powder (D)	$-2.925\cdot10^{-23}$	$1.915\cdot10^{-18}$	$-4.909\cdot10^{-14}$	$6.043\cdot10^{-10}$	$-3.225\cdot10^{-6}$	$-6.921\cdot10^{-4}$	69.0	−6.7 m/kA
Amorphous powder (E)	$-1.583\cdot10^{-23}$	$9.727\cdot10^{-19}$	$-2.295\cdot10^{-14}$	$2.498\cdot10^{-10}$	$-9.810\cdot10^{-7}$	$-4.159\cdot10^{-3}$	59.1	−3.2 m/kA

TABLE III
CIRCUIT PARAMETERS

Input voltage	V_i	50V
Output voltage	V_o	100V
Output power	P_o	500W
Duty ratio	d	0.5
Switching frequency	f_{sw}	50kHz
Switching period	T_s	20μs
Inductor average current (maximum power rating)	I_{Lave}	10A
Designed value of inductor ripple current	I_{Lpp}	5A
Inductance at I_{Lave}=10A	L_{self}	100μH

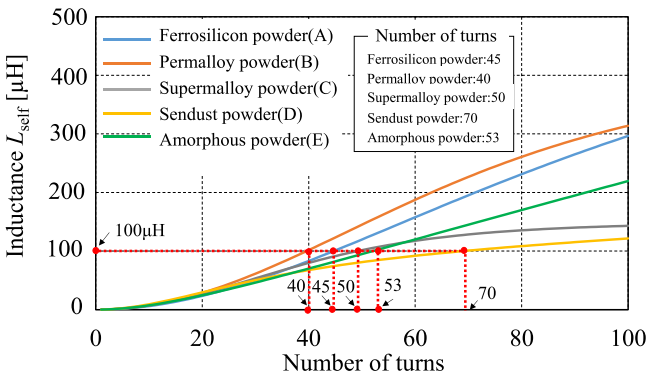

Fig. 11. Relationship between the number of turns and inductance using toroidal core shown in Table I.

Based on Faraday's law, the inductor ripple current I_{Lpp} can be obtained from Fig. 10(b) and defined as

$$I_{Lpp} \simeq \frac{V_i}{L_{\rm self}|_{i_L=I_{L\,ave}}} \cdot d \cdot T_s \tag{7}$$

where T_s is the switching period in the main switch S shown in Fig. 10(a). d is the duty ratio of S. The inductor ripples current changes non-linearly due to the non-linear behavior of relative permeability. In this design, the designed self-inductance value can be obtained using (7) and approximated at the operating point of the inductor average current $I_{L\rm ave}$. In this case, the designed inductance value is 100 μH, and as a result, the number of turns can be calculated.

Using (6), the relationship between inductance value and the number of turns in each magnetic core is shown in Fig. 11. As shown in Fig. 11, the number of turns in each magnetic core differs even though magnetic core sizes are almost the same. Therefore, the designed number of turns varies greatly depending on the magnetic properties of each core. In other words, the number of turns depends on the values of coefficients p, q, and r.

It should be noted here that the magnetic materials having high q are effective for reducing the number of turns because these materials have high relative permeability under the high current condition. In this case, core A shown in Table I is designed with 45 turns. Similarly, B is 40 turns, C is 50 turns, D is 70 turns, and E is 53 turns. The aforementioned number of turns were calculated to realize the designed inductance of 100 μH at $I_{L\rm ave} = 10$ A condition.

In the design method mentioned above, the inductance value $L_{\rm self}$ and the number of turns N are designed approximately at the operating point of $I_{L\rm ave}$ because powder cores have soft saturation property without a dramatic change of relative permeability, and this paper focuses on powder cores. However, this approximate design method at the operating point of $I_{L\rm ave}$ may not be valid in a magnetic core with strong non-linearity, such as saturable ferrite cores. For this reason, we also present an inductor current estimation method in Appendix C and a way to design the number of turns using the proposed model equation. The design method shown in Appendix C is based on applying piecewise linear calculation. Magnetic design and ripple current estimation for strong non-linear magnetic cores can be conducted using numerical analysis.

The inductor current waveforms in case of using different powder core materials with the designed number of turns under $I_{L\rm ave} = 10$ A condition are shown in Fig. 12. These waveforms are obtained based on piece-wise linear calculation. As seen in Fig. 12, the validity of the designed number of turns has been proven theoretically effective, because the inductor ripple current is almost 5A.

B. Inductance Variation

The inductance variation based on the dc current value is investigated in this section. The inductance variation depending on the dc current value can be investigated according to (6), considering the calculated number of turns. The inductance

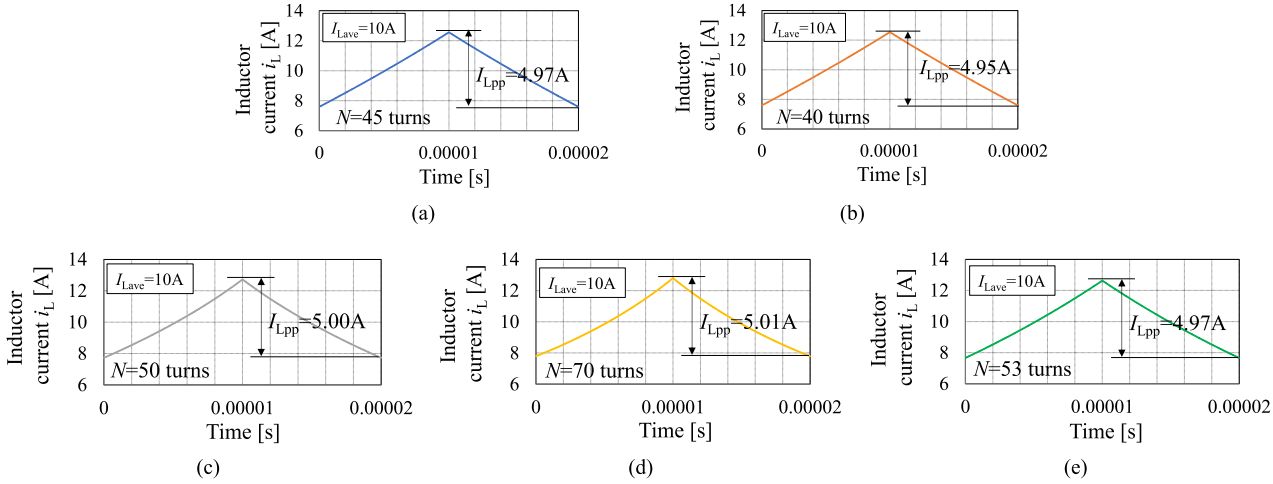

Fig. 12. Inductor ripple current estimation using piecewise linear calculation shown in Appendix C. (a) Ferrosilicon powder (A). (b) Permalloy powder (B). (c) Supermalloy powder (C). (d) Sendust powder (D). (e) Amorphous powder (E).

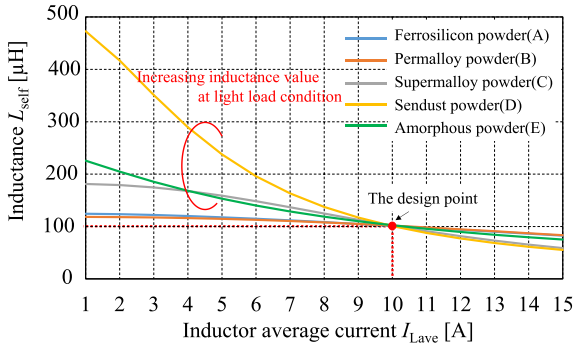

Fig. 13. Relationship between inductance value and inductor average current when using the determined number of turns.

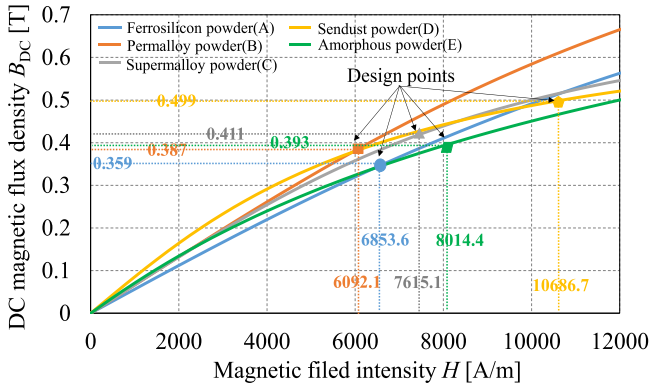

Fig. 14. Single-valued non-linear B-H curves for each core materials using (11).

variation for each inductor is shown in Fig. 13. As shown in Fig. 13, inductors utilizing cores C, D, and E can realize a higher inductance value than that of cores A and B within a light load range. A core with high initial permeability would have a high value of p [$1 + p$ means the initial permeability as shown in Fig. 7(a)], this core material tends to realize a high inductance value within light load range. Therefore, this property can improve the inductance value in the range of light loads, and it contributes to reducing conduction losses in power devices and passive components because inductor ripple current can be reduced [33].

Using non-linear inductors instead of linear inductors is popular in many industrial applications, some advantages have been reported in [47] and [48]. For instance, in passive power factor correction converters, the non-linear inductors such as powder cores can suppress generation of harmonics in input currents while downsizing magnetic components in comparison with gapped inductors using ferrite cores [47]. In dc-dc converter with maximum power point tracking for photovoltaic, the range of operation can be extended for low sun-radiation levels or partially shaded solar panels by utilizing non-linear inductor [48]. Therefore, using a non-linear inductor allows the circuit to realize a self-adaptation within a wide range of solar input power.

C. DC Magnetic Flux Density in Cores

By using the coefficients related to the relative permeability, the dc magnetic flux density can be approximately predicted. Note that the dc magnetic flux is calculated on the basis of SVBHC. Relative permeability μ_r is defined as the rate of a change of a magnetic flux density over the rate of a change of a magnetic field intensity H and divided by the space permeability. Therefore, the relative permeability can be expressed by

$$\mu_r(H) = \frac{1}{\mu_0} \cdot \frac{\partial B}{\partial H}. \tag{8}$$

From (8), the magnetic flux density $B(H)$ on SVBHC in cores can be calculated by integrating the magnetic field intensity H which can be calculated as

$$B(H) = \int_0^H \mu_r(H) \cdot \mu_0 \cdot dH. \tag{9}$$

By applying (9), the instantaneous value of flux density $B(H)$ at an instantaneous value of magnetic field intently H can be calculated. In addition, the magnetic field intensity H is a function of time because inductor currents change time by time; the dc magnetic flux density B_{dc} can be calculated by time

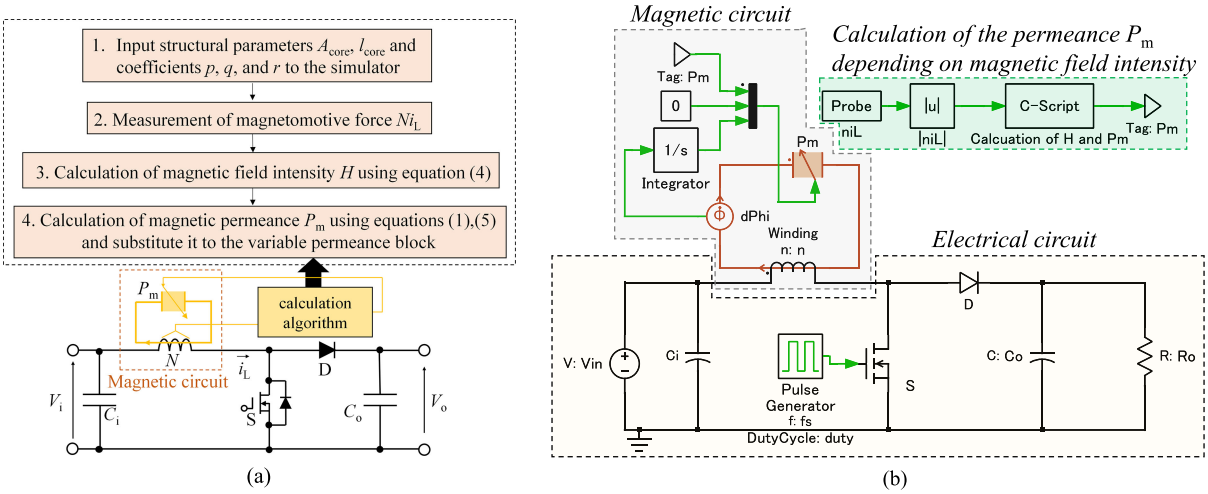

Fig. 15. Flowchart of the simulation algorithm and the simulation schematic model for the coupled analysis of electrical and magnetic circuits. (a) Flowchart of the simulation algorithm. (b) Circuit model of PLECS.

averaging for one period as follows:

$$B_{\rm dc} = \frac{1}{T_s} \cdot \int_0^{T_s} B(H) \cdot dt. \tag{10}$$

On the other hand, since applying (9) and (10) is computationally complicated, a simple calculation method of the dc magnetic flux density $B_{\rm DC}$ is also proposed as one of the approximated calculation methods. Approximated dc magnetic flux density is calculated by integrating from 0 to the average magnetic field intensity $H_{\rm ave}$ $(= NI_{L\rm ave}/l_{\rm core})$ as follows:

$$\begin{aligned} B_{\rm dc}|_{H_{\rm ave}} &\simeq \int_0^{H_{\rm ave}} \mu_r\,(H) \cdot \mu_0 \cdot dH \\ &= \int_0^{H_{\rm ave}} \left(1 + \frac{p}{1 + (H/q)^r}\right) \cdot \mu_0 \cdot dH. \end{aligned} \tag{11}$$

By solving (11), the B-H curves in each material are shown in Fig. 14. As a result, the dc flux density caused by the dc average current $I_{L\rm ave}$ can be predicted approximately. The maximum flux density $B_{\rm max}$ including half of the ac flux, which occurs by the applied voltage, is calculated as follows:

$$B_{\rm max} = B_{\rm dc} + \frac{1}{2 \cdot A_{\rm core}} \cdot \frac{V_i}{N} \cdot d \cdot T_s. \tag{12}$$

By using (12), the maximum flux density can be calculated approximately.

However, note that the dc magnetic flux density $B_{\rm dc}$, which is calculated from (11), is an approximated value. This approximated estimation method of the flux density value using (11) also may not be valid when it is applied on cores with strong nonlinearity, such as saturable ferrite cores. The reason why this approximated method cannot be applied is explained in Appendix D. Furthermore, a more accurate estimation method is presented in Appendix D.

IV. Implementation of the Proposed Model Equation to a Circuit Simulator

This section introduces an implementation method of dc superimposition characteristics of the powder core to a circuit simulator. In general, power electronics engineers use a circuit simulator in order to evaluate the whole circuits including control, power stage, and active/passive components. On the other hand, suppliers of magnetic components use electromagnetic field simulators to evaluate temperature rise, iron losses, and inductance variation of magnetic components. However, since these characteristics are related and affect each other, a comprehensive analysis method on simulators is necessary to evaluate both of power electronics circuits and magnetic components simultaneously. Certainly, there are some software that can conduct a coupled analysis of an electromagnetic field in magnetic components and circuit state; however, a highly functional computer is needed, and much time is required to calculate the electromagnetic field and circuit state simultaneously. One of the effective ways to evaluate magnetic components used in power electronics circuits is to implement magnetic core properties to a circuit simulation. In addition, accurate modeling of magnetic devices in simulation models is helpful to estimates the loss, size, and steady-state and dynamic characteristics before manufacturing the prototype.

A. Literature Review

In general, there are many implementation methods of dc superimposition characteristics to circuit simulators. For example, using the lookup table that utilizes the measured inductance can be implemented easily and the implementation procedure is simple. However, circuit designers need to carefully type the inductance values into the table in a simulator, and this work may lead to inaccuracy and it wastes a lot of time. In addition, when the number of turns is changed to adjust inductance values, the inductance has to be measured again and retyped into the simulator table.

Another method to express the dc superimposition characteristics is utilizing an equivalent circuit model using ideal passive components and current-controlled voltage source (CCVS) to reflect the current dependency, this method had been previously proposed in [49]. One of the attractive features of this method is that it allows the dc superimposition characteristics to be implemented in general circuit simulators such as SPICE by using the function of CCVS. However, this method cannot describe the physical meaning of CCVS in the equivalent circuit since inductors do not have CCVS. Furthermore, in case of a variation in the inductor specifications such as number of turns, adjusting the parameters of the circuit model is needed to coincide with the measured inductance value. Therefore, it is difficult to reflect the dc superimposition characteristics in the circuit simulator while expressing the physical meaning of variable permeability depending on inductor currents using the electrical equivalent circuit model only.

In [28], [50], and [51], equivalent circuits using electrical and magnetic circuits were proposed. To implement dc superimposition characteristic on circuit simulators, non-linear magnetic reluctances, which have current dependency, had been used. The physical meaning of inductance reduction can be reflected in the equivalent circuit by using variable magnetic reluctances.

B. Implementation Non-Linear Properties Into a Circuit Simulator

Recently, advanced multi-domain circuit simulators are becoming more popular. These multi-domain circuit simulators allow the user to simultaneously analyze not only electrical circuit, but also thermal and magnetic circuits. In this paper, PLECS (Plexim GmbH) is utilized as a software simulation tool, because it can conduct a coupled analysis of both electrical and magnetic circuits [52].

Fig. 15(a) and (b) shows the simulation algorithm flowchart for the electrical and magnetic coupled analysis and a simulation circuit model. This simulation method is easy to implement since it only changes the variable permeance while corresponding to the magnetic field intensity. Regarding the calculation algorithm inside the simulation, refer to reference [51]. In the next section, we compare the current waveforms obtained from the experimental and simulation tests, to show the validity of our proposed implementation method into the simulator.

V. Experimental and Simulated Evaluations

In this section, the experimental, theoretical, and simulation evaluations are conducted with three objectives. The first objective is to show the validity of the magnetic design method using the proposed model equation, which can fulfill the designed inductor ripple current. The second objective is to show the effectiveness of the implementation method of the dc superimposition characteristics of the powder cores into the simulator. Specifically, the non-linear inductor current waveforms obtained from simulation and experiment tests, which are compared side by side. The third objective is to provide efficiency comparison between various powder cores with the different magnetic properties and coefficients such as p, q, and r.

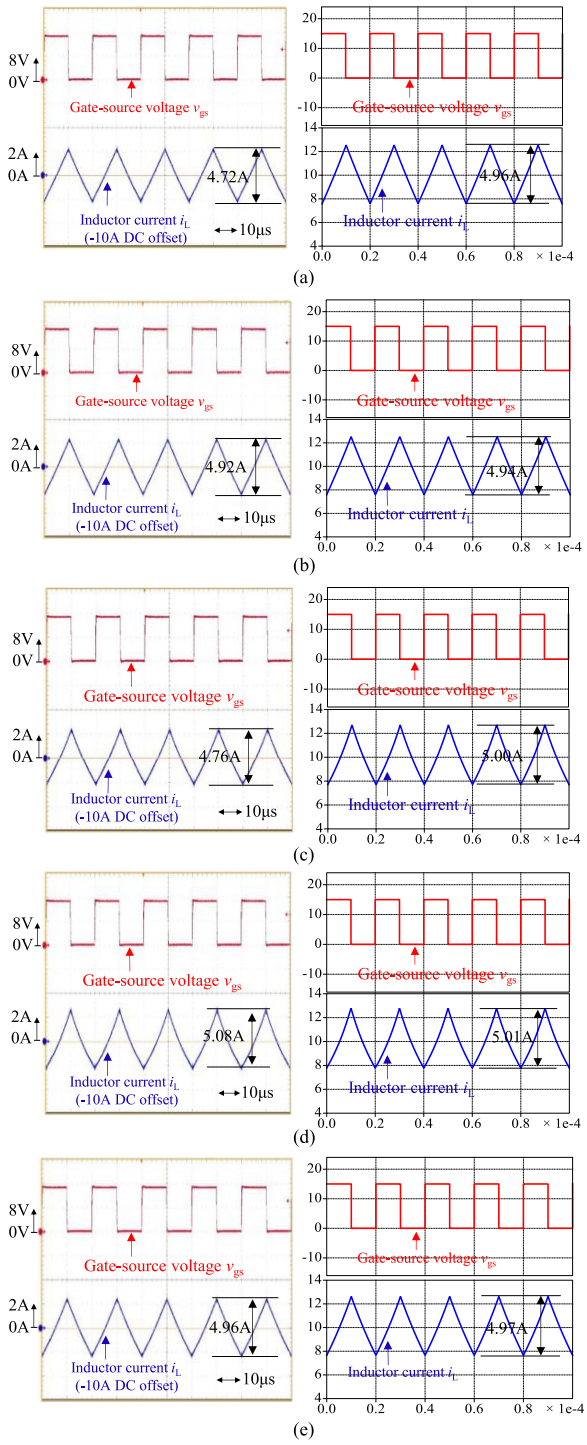

Fig. 16. Comparison of inductor current waveforms in the experiment (left side) and simulation (right side) under the condition that inductor average current is 10 A. (a) Ferrosilicon powder core (A). (b) Permalloy powder core (B). (c) Supermalloy powder core (C). (d) Sendust powder core (D). (e) Amorphous powder core (E).

A. Evaluating the Simulation Results

In order to investigate the inductance variation characteristics in each powder core, the inductor average current is intentionally changed from 10 (maximum power rating) to 6 (half load), and 3 A (light load). The comparison results of the inductor

TABLE IV
INDUCTOR RIPPLE CURRENT COMPARISON

	Inductor average current 3A				Inductor average current 6A				Inductor average current 10A			
	Experiment	Simulation	Theory (15)	Error*	Experiment	Simulation	Theory (15)	Error*	Experiment	Simulation	Theory (15)	Error*
Ferrosilicon powder (A)	4.04A	4.10A	4.12A	-1.46%	4.20A	4.37A	4.38A	-3.89%	4.72A	4.96A	4.97A	-4.84%
Permalloy powder (B)	4.24A	4.26A	4.28A	-0.47%	4.52A	4.45A	4.45A	1.57%	4.92A	4.94A	4.95A	-0.40%
Supermalloy powder (C)	3.04A	2.88A	2.88A	5.55%	3.48A	3.40A	3.40A	2.35%	4.76A	5.00A	5.00A	-4.80%
Sendust powder (D)	1.60A	1.43A	1.43A	11.89%	2.80A	2.60A	2.57A	7.69%	5.08A	5.01A	5.01A	1.39%
Amorphous powder (E)	2.96A	2.76A	2.76A	7.24%	3.80A	3.64A	3.64A	4.40%	4.96A	4.97A	4.97A	-0.20%

*The error percentages are calculated by (experimental value—simulation value)/simulation value.

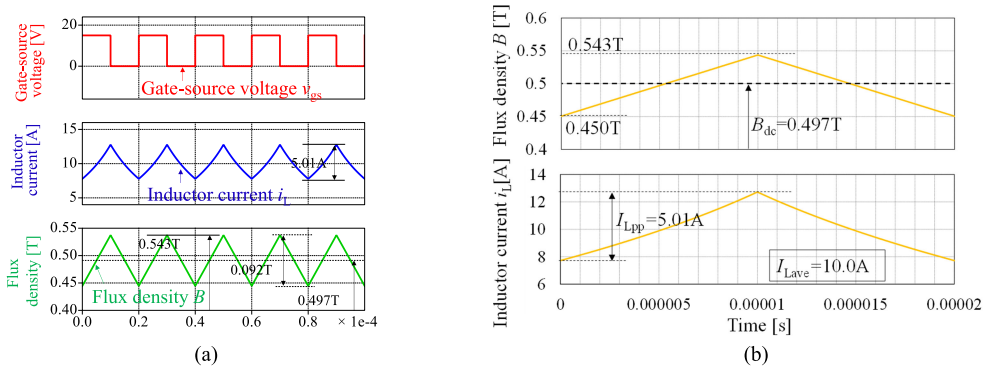

Fig. 17. Magnetic flux waveform when using the sendust powder cores. The simulation condition is that inductor average current is 10 A. (a) Simulation results. (b) Theoretical analysis results using piecewise linear calculation according to (9), (10), and (15).

ripple currents in the experiment and simulation are summarized in Table IV. As shown in Table IV, the experimental results are consistent with the simulation results. In addition to this, theoretical values using (15) shown in Appendix C are also listed in Table IV, and these values are consistent with the experimental and simulation results. Therefore, it has been proven that the proposed modeling method is accurate and effective.

B. Ripple Current Waveform Comparison Under DC Current Superimposed Condition and Validation of the Design Method

Fig. 16 shows the experimental results when the cores A–E have the designed number of turns. These experimental results are measured while setting the dc offset of minus 10 A to show the ripple currents clearly. As shown in Fig. 16, the designed ripple current of 5 A and the measured inductor ripple currents are almost identical with each other. It can be noticed that the experimental inductor current waveform when using the sendust cores (D) changes non-linearly rather than linear triangular wave current, and this waveform is accurately reproduced by circuit simulation.

C. Validation of Magnetic Flux Density Waveform on Simulation

The above discussions were only focused on the current behavior under the dc superimposition condition. Then, the magnetic flux densities in powder cores are evaluated through simulation tests. The advantage of a coupled analysis of electrical and magnetic circuits also includes the simultaneous observation of electrical and magnetic behaviors. The point for discussion in this section is whether the theoretical value calculated by (11) and (12) and the simulation values are consistent or not. In addition to this, theoretical value using (9), (10), and (15) on the basis of piecewise linear calculation shown in Appendix C is compared. Fig. 17(a) and (b) shows the simulation magnetic flux waveform and theoretical waveforms using (9), (10), and (15) when using the sendust powder cores (D). The pre-condition for the inductor average current is 10 A. Table V shows magnetic flux density comparison results among the simulation and approximated theoretical values using (11) and (12) and theoretical values using (9), (10), and (15). As seen in Table V, the theoretical values and simulation values are almost identical with each other.

D. Evaluation of Power Conversion Efficiency

Finally, power conversion efficiencies when the load changes between light to heavy load were obtained. The measured power conversion efficiencies are shown in Fig. 18. It can be deduced that the core E inductor has a better power conversion efficiency in the light load range because of its low-iron loss characteristics. On the other hand, at heavy load condition around 10 A, Core B has the highest power conversion efficiency because it has few winding turns, which minimizes the copper loss compared with other inductors.

VI. CONCLUSION

This paper proposed the modeling, design, and simulation methods for powder cores with non-linear inductance characteristics. An accurate model of the non-linear relative permeability

TABLE V
FLUX DENSITY COMPARISON BETWEEN SIMULATION AND THEORY

	Condition: Inductor average current 10A							
	Average flux density B_{dc}				Maximum flux density B_{max}			
	Simulation	Theory [Approximation by H_{ave}, (11)]	Theory [using (9)-(10) and (15)]	Error*	Simulation	Theory [Approximation by H_{ave}, (11)]	Theory [using (9)-(10) and (15)]	Error*
Ferrosilicon powder (A)	0.358T	0.359T	0.358T	0.279%	0.436T	0.437T	0.436T	0.229%
Permalloy powder (B)	0.385T	0.387T	0.385T	0.519%	0.471T	0.472T	0.471T	0.212%
Supermalloy powder (C)	0.407T	0.411T	0.408T	0.982%	0.474T	0.478T	0.475T	0.844%
Sendust powder (D)	0.497 T	0.499T	0.497T	0.402%	0.543T	0.546T	0.543T	0.552%
Amorphous powder (E)	0.392T	0.393T	0.392T	0.255%	0.454T	0.456T	0.454T	0.440%

*The error percentages are calculated by Theoretical value [Approximation by H_{ave}, (11)]—Simulation value/Simulation value.

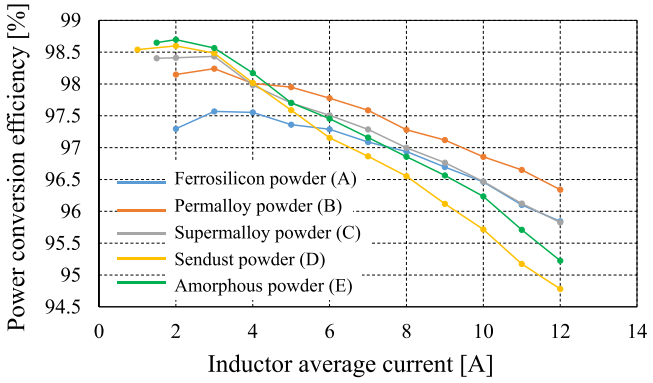

Fig. 18. Power conversion efficiency from light to heavy loads.

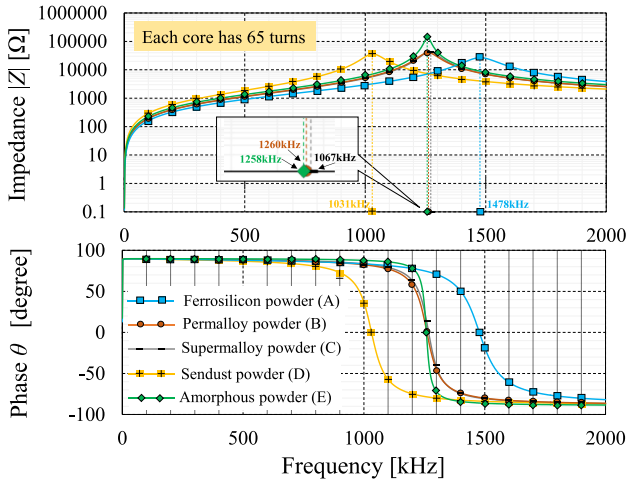

Fig. 19. Impedance characteristics of DUT when measuring the relative permeability. Note that dc current zero condition.

had been proposed. The proposed model equation showing the relative permeability has only three coefficients and they can be extracted through a simple experimental test. Furthermore, the design for powder core and implementation methods into circuit simulator has been reported. The proposed analysis has been evaluated through the simulation and experimental tests, and the proposed model has been proven accurate and effective. As future works, the proposed magnetic device model will be applied into resonant converters such as *LLC* resonant converters or the integrated magnetics [53] using non-linear magnetic models used for interleaved boost converters.

APPENDIX

A. Measurement Results of SRF in Each DUT (65 Turns)

The self-resonant frequencies in each core are measured to investigate the influence of parasitic capacitance between windings in advance when measuring the relative permeability as previously explained in Section II-C. The measurements had been obtained by using impedance analyzer (KEYSIGHT TECHNOLOGIES, Model: E4990A). Fig. 19 shows the magnitude of impedance |Z| and the phase θ in each DUT. As seen in Fig. 19, the self-resonant frequencies in each core are almost in the range between 1 and 1.5 MHz. In addition, the measured frequency while obtaining dc superimposition characteristics is 50 kHz. Therefore, the influence of parasitic capacitance on the measurement accuracy is low because the measured frequency (50 kHz) is 20 times lower than the SRF. Therefore, the influence of parasitic capacitance on the measurement can be neglected. On the other hand, when measuring dc superimposition characteristics, self-inductance gradually decreases in accordance with increasing dc current value. In this case, SRF increases because the measured self-inductance gradually decreases in accordance with increasing dc current value. Thus, even during dc superimposed measurement, the parasitic capacitance has no effect on the accurate measurements.

B. Confirmation of the Validity of the Coefficient r in Each Core

In this section, the validities of the coefficient of *r* value shown in Table II are confirmed. To confirm the validity of the *r* values obtained by computer calculation, the behavior of approximated lines is illustrated by the proposed model equation when *r* value is varied. Fig. 20(a) shows the comparison results when *r* values are slightly varied in the case of the sendust core (D). The *r* value is varied within $\pm 10\%$ from the specified value ($r = 1.91$). It can be noticed that when the *r* value is changed from the specified value ($r = 1.91$), the errors between the measured results and theoretical values increase. To clarify the relative error value between measured and theoretical values, Fig. 20(b) shows the relative error. The relative error is calculated by using the following equation:

$$\text{Relative Error} = \frac{|\text{Theoretical value} - \text{Measured value}|}{\text{Measured value}}. \tag{13}$$

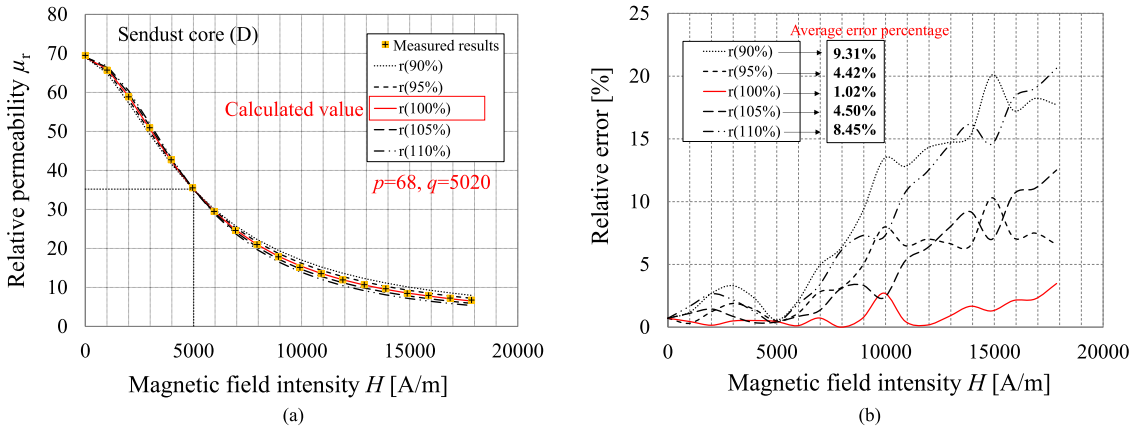

Fig. 20. Comparison results and relative error of the measured and theoretical value when *r* values are varied [Sendust cores (D)]. (a) Comparison results when varying r value under the condition that the p and q are fixed. (b) Relative error from measured results.

TABLE VI
AVERAGE RELATIVE ERROR PERCENTAGE WHEN *R* VALUE IS CHANGED

Average error percentage [%]	*r* is varied between 90%~110%				
	r (90%)	*r* (95%)	*r* (specified value)	*r* (105%)	*r* (110%)
Ferrosilicon powder (A) (p=43.9, q=14300)	1.74% (r=1.75)	0.98% (r=1.84)	0.51% (r=1.94)	0.79% (r=2.04)	1.40% (r=2.13)
Permalloy powder (B) (p=51.9, q=13100)	2.39% (r=2.10)	1.48% (r=2.21)	0.84% (r=2.33)	0.97% (r=2.45)	1.59% (r=2.56)
Supermalloy powder (C) (p=50.1, q=8260)	5.05% (r=2.23)	2.79% (r=2.35)	1.16% (r=2.47)	2.71% (r=2.59)	4.92% (r=2.71)
Sendust powder (D) (p=68, q=5020)	9.31% (r=1.71)	4.42% (r=1.81)	1.02% (r=1.91)	4.50% (r=2.01)	8.45% (r=2.11)
Amorphous powder (E) (p=58.1, q=6020)	4.36% (r=1.12)	2.28% (r=1.18)	1.17% (r=1.24)	2.31% (r=1.30)	3.85% (r=1.36)

As seen in Fig. 20(b), the relative errors increase in accordance with the great change in the *r* value, from the specified values. The average relative error becomes large when the *r* value is greatly changed from the specified value ($r = 1.91$). Table VI shows the averaged relative error when *r* values in each core is changed from the specified value. As seen in Table VI, the specified value has good accuracy. Therefore, the validity of the specified value of *r* can be confirmed.

C. Theoretical Method for Estimating Strong Non-Linear Current by Piecewise Linear Calculation

If the relative permeability μ_r is dramatically changed in one period in a core with strong non-linear characteristics such as saturable ferrite core, there is a possibility that actual inductor ripple current does not match with calculated results using both (6) and (7). In this section, the theoretical estimation method for strong non-linear current is introduced using the proposed model equation. In general, inductor ripple current is a function of time according to Faraday's law ($V_L = L_{\rm self} \cdot di/dt$). On the other hand, the non-linear inductance or the relative permeability is a function of instantaneous inductor current value $L(i_L)$ as shown in (6). To solve this case, inductor current can be estimated by piecewise linear calculation. Fig. 21(a) shows the concept of the piecewise linear calculation, where the schematic diagram of the non-linear inductor current is presented. I_0 is the initial value of the current at time t_0 and is assumed as the bottom of the inductor current. The inductance value is calculated by L_0 and its value is calculated by (6) using I_0. The inductor current I_1 at t_1 after time step Δt from t_0 is calculated by the sum of initial value I_0 and ripple current during Δt on the basis of the Faraday's law. In the same way, inductor currents I_2 and I_3 are also calculated. By calculating up to on-period of S shown in Fig. 10(a), inductor ripple current with strong nonlinearity are estimated. The above concept can be summarized by the following equation:

$$\begin{cases} I_0|_{t=t_0} = I_0 \\ I_1|_{t=t_1} = I_0 + \dfrac{V_L}{L_0|_{i_L=I_0}} \cdot (t_1 - t_0) = I_0 + \dfrac{V_L}{L_0|_{i_L=I_0}} \cdot \Delta t \\ I_2|_{t=t_2} = I_1 + \dfrac{V_L}{L_1|_{i_L=I_1}} \cdot (t_2 - t_1) = I_1 + \dfrac{V_L}{L_1|_{i_L=I_1}} \cdot \Delta t \\ I_3|_{t=t_3} = I_2 + \dfrac{V_L}{L_2|_{i_L=I_2}} \cdot (t_3 - t_2) = I_2 + \dfrac{V_L}{L_2|_{i_L=I_2}} \cdot \Delta t \end{cases} \tag{14}$$

where V_L is the applied voltage of inductor. In case of the boost converter as shown in Fig. 10(a), V_L equal input voltage V_i during on-state of main switch S. During off-state, V_L is equal the difference of input and output voltage ($V_L = V_i - V_o$). The generalized equation of (14) is shown by the following equation:

$$\begin{cases} I_0|_{t=t_0} = I_0 \\ I_n|_{t=t_n} = I_{n-1} + \dfrac{V_L}{L_{n-1}} \cdot (t_n - t_{n-1}) = I_{n-1} + \dfrac{V_L}{L_{n-1}} \cdot \Delta t \\ L_{n-1} = \dfrac{N^2 \cdot \mu_0 \cdot A_{\rm core}}{l_{\rm core}} \cdot \left(1 + p/\left(1 + \left(\dfrac{N \cdot I_{n-1}/l_{\rm core}}{q}\right)^r\right)\right) \\ I_{L\rm ave} = \dfrac{1}{T_s} \cdot \int_0^{T_s} I(t)\, dt \\ I_{Lpp} = I_{L\max} - I_0 \\ n = 1, 2, 3, 4, 5 \cdots \end{cases} \tag{15}$$

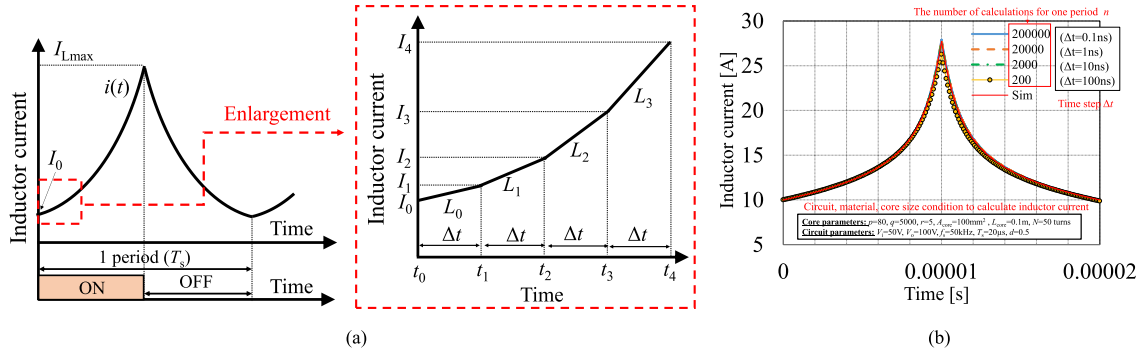

Fig. 21. Estimating nonlinear current by discretization. (a) Calculation method using numerical analysis and discretization calculation. (b) Comparison between theoretical analysis and simulation.

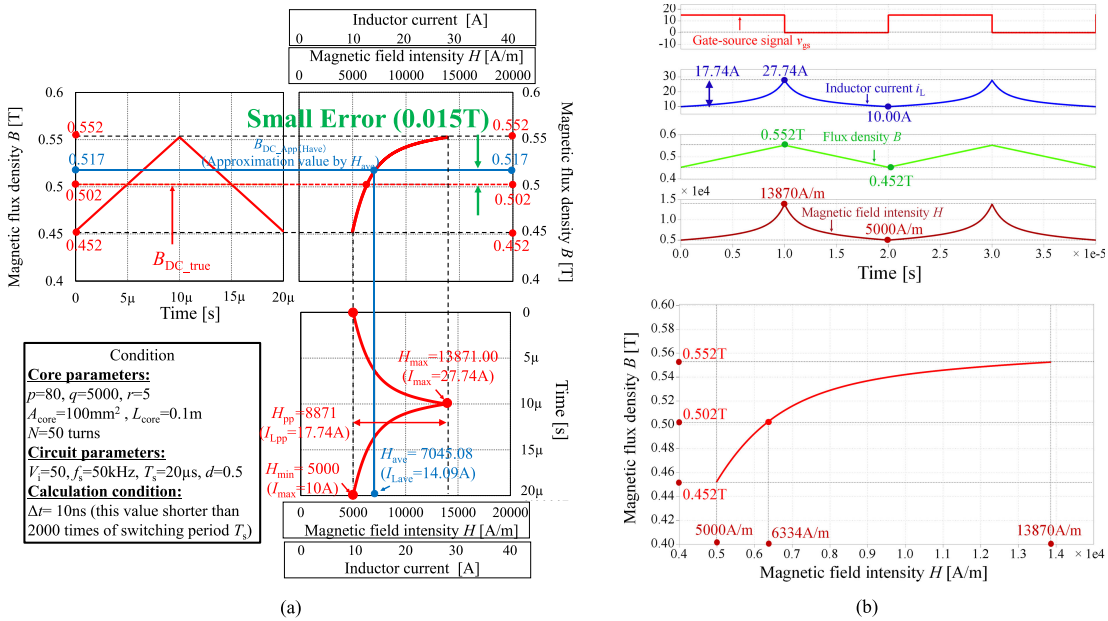

Fig. 22. Comparison between a calculation method non-linear current by numerical analysis and discretization and simulation using proposed magnetic device model. (a) Theoretical derived B-H curve using (9), (10), and (15). (b) Simulated waveform and B-H curve.

TABLE VII
COMPARISON BETWEEN THEORETICAL ANALYSIS AND SIMULATION UNDER THE STRONGER NON-LINEAR CORES

	Theoretical analysis (using calculation method using (15))		Simulation
Inductor ripple current	17.74 A		17.74A
Average flux density B_{dc}	Calculation by H_{ave} (Using eq. (11))	Calculation by B-H curve (Using eq. (9)-(10), (15))	0.502T
	0.517T	0.502T	

where I_{Lave} is the inductor average current and it can be obtained by time averaging for one period. I_{Lpp} is calculated by the difference between maximum inductor current I_{Lmax} for one period and I_0. By using the above equation and selecting the fairly shorter time step Δt than switching period T_s, the estimation of the behavior of non-linear current is possible even in case of a core with a strong non-linearity. As an approximated calculation method for inductor ripple current including strong non-linear behavior, Capua *et al.*'s study [31] is one of the interesting ones. The purpose of the calculation method proposed in [31] is to estimate the inductor ripple current based on dividing the operations region into weak saturation, roll-off, deep saturation regions, in the case of ferrite cores including saturation operation. However, to estimate ripple current value in saturable ferrite inductors, some coefficients have to be obtained from the inductance versus current map, which divides operation region into weak saturation, roll-off, deep saturation regions. Nonetheless, the advantage of the proposed calculation method using (15) is that it can be directly applied using the model equation shown in (5). It is worth mentioning that the ripple current can be calculated directly from the material parameters (p, q, r) and it helps in designing the number of turns. From the magnetic material selection perspective, the proposed ripple current estimation method is helpful to se-

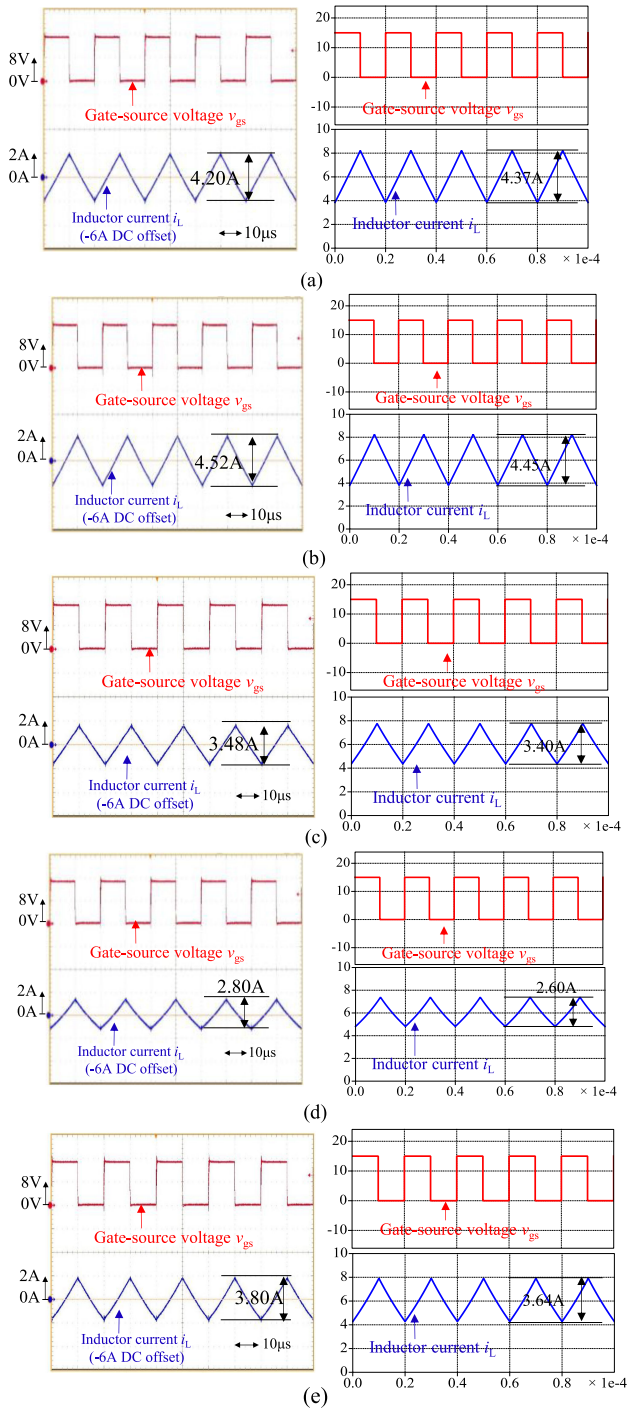

Fig. 23. Comparison of inductor current waveforms in the experiment (left side) and simulation (right side) under the condition that inductor average current is 6 A. (a) Ferrosilicon powder core (A). (b) Permalloy powder core (B). (c) Supermalloy powder core (C). (d) Sendust powder core (D). (e) Amorphous powder core (E).

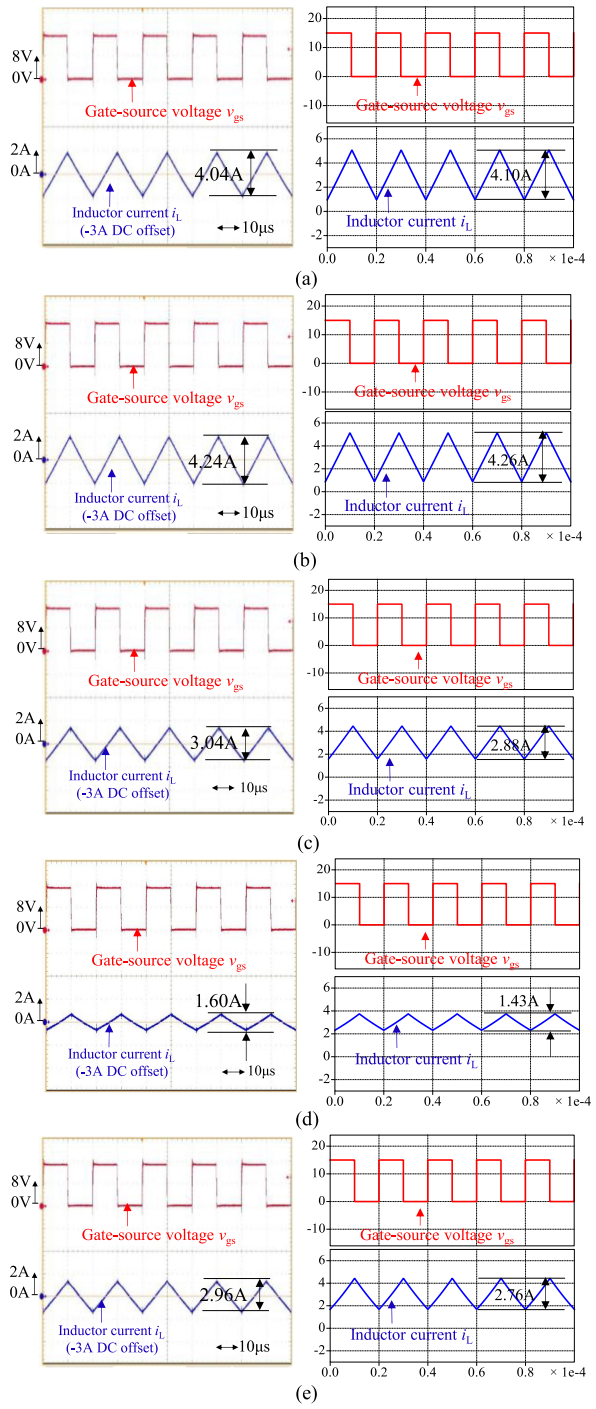

Fig. 24. Comparison of inductor current waveforms in the experiment (left side) and simulation (right side) under the condition that inductor average current is 3 A. (a) Ferrosilicon powder core (A). (b) Permalloy powder core (B). (c) Supermalloy powder core (C). (d) Sendust powder core (D). (e) Amorphous powder core (E).

lect the proper magnetic material from several types of powder cores.

To evaluate the calculation method based on piecewise linear calculation, the current waveforms are compared with the simulation waveform. Fig. 21(b) shows the comparison results of calculated values using (15) and simulation. As a precondition to illustrate non-linear inductor current, the material, circuit, and calculation parameters shown in Fig. 21(b) are used, and I_0 used in (15) is set as 10 A. The core material is assumed that it has strong non-linearity in comparison with powder cores used in this paper because slope of r is much higher than that of the materials shown in Table II. As seen in Fig. 21(b), when selecting

the time step Δt of 100 ns for (15), high error between simulation waveform and theoretical analysis is expected. However, when selecting the shorter time step Δt, theoretical analysis and simulation results are consistent with each other. Therefore, just by creating a design tool on the basis of (15), ripple current and number of winding turns can be estimated and designed by utilizing numerical analysis even in case of using magnetic cores with strong non-linearity.

D. Calculation Method of DC Flux Density $B_{\rm dc}$ of Strong Non-Linear Core and Error Due to Approximated Value of $H_{\rm ave}$

In this section, a calculation method of dc flux density $B_{\rm dc}$ when using a core with strong non-linearity is proposed. Moreover, the cause of error due to approximated values of $H_{\rm ave}$ is presented as a case study. In this paper, the dc flux density in the presented mathematical analysis was calculated and approximated by using "average" magnetic field intensity $H_{\rm ave}\ (= N \cdot I_{L\rm ave}/l_{\rm core})$ as shown in (11). However, in case of a core with strong non-linear characteristics such as saturable ferrite core, the calculated dc flux density using (11) would have a small error. To explain the reason behind this error, Fig. 22(a) shows a B-H curve derived theoretically using (9), (10), and (15). As a precondition to illustrate a B-H curve, the material, circuit, and calculation parameters shown in Fig. 22(a) are used, and I_0 used in (15) is set as 10 A. The core material is assumed that it has strong non-linearity in comparison with powder cores used in this paper because r value is much higher than that of the materials shown in Table II. The calculation procedure is as follow: First, inductor current is calculated by using (15), then, the magnetic field intensity is calculated by (4). Finally, magnetic flux density B (H) based on SVBHC is calculated using (9). As seen in this Fig. 22(a), the amplitude of inductor ripple current is 17.74 A and the inductor ripple current includes strong non-linear behavior. In this case, the "average" magnetic field intensity $H_{\rm ave}$ is 7045.08 A/m $(I_{L\rm ave} = 14.09\ \rm A)$ and the calculated dc magnetic flux density $B_{\rm dc\_app(Have)}$ using (11) is 0.517 T. However, by alloctaing the actual average flux density $B_{\rm dc\_true}$ on this B-H curve shown in Fig. 22(a), the value is estimated as 0.502 T. Therefore, there is the small error between actual value and approximated value using $H_{\rm ave}$. That error of dc flux density occurs because it was calculated by "average magnetic intensity $H_{\rm ave}$" and the inductor ripple current has strong non-linearity. However, when using the proposed magnetic device model used in simulation, dc flux density can be predicted on the simulation. Fig. 22(b) shows the simulation results using the material and circuit parameters shown in Fig. 22(a). As seen in Fig. 22(b), when investigating actual dc magnetic flux density $B_{\rm dc\_true}$ on the simulation result, it is 0.502T, and this value matches with the theoretically derived value using (9), (10), and (15).

The conclusion of this section is that the estimation of dc flux density $B_{\rm dc}$ by $H_{\rm ave}$ introduces errors when the nonlinearity of cores is strong. The comparison results are shown in Table VII. In this case, while determining average flux density, using (9), (10), and (15) is recommended instead of using (11) and (12).

E. Measurement Results of Ripple Current Under the Low and Middle DC Current Condition

The simulation and experimental waveforms under the conditions that inductor average currents are 6 and 3 A are shown in Figs. 23 and 24, respectively.

REFERENCES

[1] K. Mainali and R. Oruganti, "Conducted EMI mitigation techniques for switch-mode power converters: A survey," *IEEE Trans. Power Electron.*, vol. 25, no. 9, pp. 2344–2356, Sep. 2010.

[2] H. Funato, T. Mori, T. Igarashi, S. Ogasawara, F. Okazaki, and Y. Hirota, "Optimization of switching transient waveform to reduce harmonics in selective frequency bands," *IEEJ J. Ind. Appl.*, vol. 2, no. 3, pp. 161–169, May 2013.

[3] M. Kącki, M. S. Ryłko, J. G. Hayes, and C. R. Sullivan, "Magnetic material selection for EMI filters, " in *Proc. IEEE Energy Convers. Congr. Expo.*, Oct. 2017, pp. 2350–2356.

[4] Y. Itoh, S. Kimura, J. Imaoka, and M. Yamamoto, "Inductor loss analysis of various materials in interleaved boost converters," in *Proc. IEEE Energy Convers. Congr. Expo.*, Sep. 2014, pp. 980–987.

[5] M. S. Rylko, K. J. Hartnett, J. G. Hayes, and M. G. Egan, "Magnetic material selection for high power high frequency inductors in DC-DC conversion," in *Proc. IEEE Appl. Power Electron. Conf. Expo.*, Feb. 2009, pp. 2043–2049.

[6] M. S. Rylko, B. J. Lyons, J. G. Hayes, and M. G. Egan, "Revised magnetics performance factors and experimental comparison of high-flux materials for high-current DC-DC inductors," *IEEE Trans. Power Electron.*, vol. 26, no. 8, pp. 2112–2126, Aug. 2011.

[7] A. J. Hanson, J. A. Belk, S. Lim, C. R. Sullivan, and D. J. Perreault, "Measurements and performance factor comparisons of magnetic materials at high frequency," *IEEE Trans. Power Electron.*, vol. 31, no. 11, pp. 7909–7925, Nov. 2016.

[8] A. Williams, V. Moruzzi, A. Malozemoff, and K. Terakura, "Generalized Slater-Pauling curve for transition-metal magnets," *IEEE Trans. Magn.*, vol. MAG-19, no. 5, pp. 1983–1988, Sep. 1983.

[9] Magnetics, Ferrite Materials: Ferrite Cores, 2018. [Online]. Available: https://www.mag-inc.com/Products/Ferrite-Cores

[10] TDK Corporation, Mn-Zn Ferrite Material Characteristics, 2018. [Online]. Available: https://product.tdk.com/info/en/catalog/datasheets/ferrite_mn-zn_material_characteristics_en.pdf

[11] TDK Corporation, 2018. Ni-Zn Material Characteristics [Online]. Available: https://product.tdk.com/info/en/catalog/datasheets/ferrite_ni-zn_material_characteristics_en.pdf

[12] Hitachi Metals, Ltd., 2018, Soft Ferrites, [Online]. Available: http://www.hitachi-metals.co.jp/e/products/elec/tel/p13_21.html

[13] JFE Ferrite Corporation, 2018, FERRITE MATERIALS FOR POWER SUPPLY, [Online]. Available: http://www.jfe-frt.com/products/pdf/004.pdf

[14] Magnetics, 2018, Powder Cores. [Online]. Available: https://www.mag-inc.com/Products/Powder-Cores

[15] ALPS ELECTRIC CO., LTD., 2018, LiqualloyTM Toroidal Coil Technical Data Sheet. [Online]. Available: https://www.alps.com/prod/info/E/HTML/Toroidal/Toroidal/GLT1/datasheet_GLT1.pdf

[16] POCO Magnetic Co., Ltd, 2018, Powder cores, [Online]. Available: http://pocomagnetic.com/en/product/index94.html

[17] Ueno Co., Ltd., 2018, Power circuit components, [Online]. Available: http://www.uenokk.co.jp/en/product/power_supply/

[18] Q. Li, Y. Dong, F. C. Lee, and D. J. Gilham, "High power density low-profile coupled inductor design for integrated point of load converter," *IEEE Trans. Power Electron.*, vol. 28, no. 1, pp. 547–554, Jan. 2013.

[19] W. G. Odendaal, J. Azevedo, G. W. Brüning, and R. M. Wolf, "A high-efficiency magnetic component with superior caloric performance for low-profile high-density power conversion," *IEEE Trans. Ind. Appl.*, vol. 40, no. 5, pp. 1287–1293, Sep. 2004.

[20] Y. Wang, G. Calderon-Lopez, and A. J. Forsyth, "High-frequency gap losses in nanocrystalline cores," *IEEE Trans. Power Electron.*, vol. 32, no. 6, pp. 4683–4690, Jun. 2017.

[21] S. Nogawa, M. Kuwata, T. Nakau, D. Miyagi, and N. Takahashi, "Study of modeling method of lamination of reactor core," *IEEE Trans. Magn.*, vol. 42, no. 4, pp. 1455–1458, Apr. 2006.

[22] J. Muhlethaler, J. W. Kolar, and A. Ecklebe, "A novel approach for 3D air gap reluctance calculations," in *Proc. 8th Int. Conf. Power Electron. ECCE Asia*, May 2011, pp. 446–452.
[23] R. Jez, "Influence of the distributed air gap on the parameters of an industrial inductor," *IEEE Trans. Magn.*, vol. 53, no. 11, Nov. 2017, Art. no. 8401605.
[24] T. Tera, H. Taki, and T. Shimizu, "Loss reduction of laminated core inductor used in on-board charger for EVs," *IEEJ J. Ind. Appl.*, vol. 4, no. 5, pp. 626–633, Sep. 2015.
[25] K. Kabeya, S. Yanase, Y. Okazaki, and K. Yun, "Magnetic property of iron-dust cores with mixture of ferromagnetic ferrite powder and alumina powder," *IEEE Trans. Magn.*, vol. 50, no. 4, Apr. 2014, Art. no. 2800504.
[26] K. Shiroki, K. Kawano, H. Matsuura, and H. Kishi, "New type metal composite material for SMD power inductor," *J. Jpn. Soc. Powder Powder Metallurgy*, vol. 61, no. S1, pp. S242–S244, May 2014.
[27] P. Nakmahachalasint, K. D. T. Ngo, and L. Vu-Quoc, "A static hysteresis model for power ferrites," *IEEE Trans. Power Electron.*, vol. 17, no. 4, pp. 453–460, Jul. 2003.
[28] M. Luo, D. Dujic, and J. Allmeling, "Modeling frequency independent hysteresis of ferrite core materials using permeance-capacitance analogy for system-level circuit simulations," *IEEE Trans. Power Electron.*, vol. 33, no. 12, pp. 10055–10070, Dec. 2018.
[29] J. D. Pollock, W. Lundquist, and C. R. Sullivan, "Predicting inductance Roll-Off with DC excitations," in *Proc. IEEE Energy Convers. Congr. Expo.*, Sep. 2011, pp. 2139–2145.
[30] G. R. C. Mouli, J. Schijffelen, P. Bauer, and M. Zeman, "Estimation of ripple and inductance roll off when using powdered iron core inductors," in *Proc. Int. Exhib. Conf. Power Electron., Intell. Motion, Renew. Energy Energy Manage.*, May 2016, pp. 1383–1390.
[31] G. D. Capua, N. Femia, and K. Stoyka, "Switching power supplies with ferrite inductors in sustainable saturation operation," *Int. J. Electr. Power Energy Syst.*, vol. 93, pp. 494–505, Dec. 2017.
[32] L. Liu *et al.*, "Design and additive manufacturing of multi-permeability magnetic cores," in *Proc. IEEE Energy Convers. Congr. Expo.*, Oct. 2017, pp. 881–886.
[33] L. Wang, Z. Hu, Y. F. Liu, Y. Pei, X. Yang, and Z. Wang, "A horizontal-winding multi permeability LTCC inductor for a low-profile hybrid DC/DC converter," *IEEE Trans. Power Electron.*, vol. 28, no. 9, pp. 4365–4375, Jun. 2017.
[34] J. Imaoka *et al.*, "Feasible evaluations of coupled multilayered chip inductor for POL converters," *IEEJ J. Ind. Appl.*, vol. 4, no. 3, pp. 126–135, May 2015.
[35] Y. Su, Q. Li, and F. C. Lee, "Design and evaluation of a high-frequency LTCC inductor substrate for a three-dimensional integrated DC/DC converter," *IEEE Trans. Power Electron.*, vol. 28, no. 9, pp. 4354–4364, Sep. 2013.
[36] Q. Li and F. C. Lee, "High inductance density low-profile inductor structure for integrated point-of-load converter," in *Proc. IEEE Appl. Power Electron. Conf. Expo.*, Feb. 2009, pp. 1011–1017.
[37] D. Hou, F. C. Lee, and Q. Li, "Very high frequency IVR for small portable electronics with high-current multiphase 3-D integrated magnetics," *IEEE Trans. Power Electron.*, vol. 32, no. 11, pp. 8705–8717, Nov. 2017.
[38] Y. Su, Q. Li, F. C. Lee, D. Hou, and S. She, "Planar inductor structure with variable flux distribution —A benefit or impediment?" in *Proc. IEEE Appl. Power Electron. Conf. Expo.*, Mar. 2015, pp. 1169–1176.
[39] E. Cardelli, E. Della Torre, and E. Pinzaglia, "Identifying the preisach function for soft magnetic materials," *IEEE Trans. Magn.*, vol. 39, no. 3, pp. 1341–1344, May 2003.
[40] J. R. Brauer, "Simple equations for the magnetization and reluctivity curves of steel," *IEEE Trans. Magn.*, vol. 11, no. 1, p. 81, Jan. 1975.
[41] J. Marcos Alonso, G. Mart´ınez, M. Perdigao, M. Rafael Cosetin, and R. N. do Prado, "A systematic approach to modeling complex magnetic devices using SPICE: Application to variable inductors," *IEEE Trans. Power Electron.*, vol. 31, no. 11, pp. 7735–7746, Nov. 2016.
[42] ROHM Co., Ltd., 2018, SiC Power Module, [Online]. Available: https://www.rohm.com/products/sic-power-devices/sic-power-module
[43] GaN Systems Inc., 2018, GaN Transistors. [Online]. Available: https://gansystems.com/gan-transistors/
[44] ABB Ltd., 2018, ABB semiconductor simulation tool. [Online]. Available: https://new.abb.com/docs/librariesprovider109/default-document-library/semis/semis_user-manual.pdf?sfvrsn=6
[45] J. Imaoka, K. Okamoto, M. Shoyama, Y. Ishikura, M. Noah, and M. Yamamoto, "Modeling, magnetic design, and simulation methods considering DC superimposition characteristic of powder cores used in power converters," in *Proc. Int. Power Electron. Conf.*, May 2018, pp. 1095–1102.
[46] HIOKI E.E. CORPORATION, 2018, LCR METER IM3523, [Online]. Available: https://www.hioki.com/en/products/detail/?product_key=5790.
[47] W. H. Wölfle and W. G. Hurley, "Quasi-active power factor correction with a variable inductive filter: Theory, design and practice," *IEEE Trans. Power Electron.*, vol. 18, no. 1, pp. 248–255, Jan. 2003.
[48] L. Zhang, W. G. Hurley, and W. H. Wölfle, "A new approach to achieve maximum power point tracking for PV system with a variable inductor," *IEEE Trans. Power Electron.*, vol. 26, no. 4, pp. 1031–1037, Apr. 2011.
[49] Murata Manufacturing Co., Ltd., An Equivalent Circuit Model Reflecting the Current Dependency of Power Inductors and Evolving Simulations of Power Supply Circuits, 2018. [Online]. Available: https://www.murata.com/en-global/about/newsroom/techmag/metamorphosis18/appnote/01
[50] O. Ichinokura, K. Sato, T. Jinzenji, and K. Tajima, "A spice model of porthogonal-core transformers," *J. Appl. Phys.*, vol. 69, no. 8, pp. 4928–4930, Apr. 1991.
[51] J. Allmeling, W. Hammer, and J. Schonberger, "Transient simulation of magnetic circuits using the permeance-capacitance analogy," in *Proc. IEEE 13th Workshop Control Model. Power Electron.*, Jun. 2012, pp. 1–6.
[52] Plexim, 2018. [Online]. Available: https://www.plexim.com/plecs
[53] J. Imaoka *et al.*, "Magnetic design method considering DC-biased magnetization for integrated magnetic components used in multiphase boost converters," *IEEE Trans. Power Electron.*, vol. 33, no. 4, pp. 3346–3362, Apr. 2018.

Jun Imaoka (S'11–M'15) received the M.S. and Ph.D. degrees in electronic function and system engineering from Shimane University, Matsue, Japan, in 2013 and 2015, respectively.

From October 2015 to March 2018, he was with Kyushu University, Fukuoka, Japan, as an Assistant Professor. He is currently an Assistant Professor with Nagoya University, Nagoya, Japan. His research interests include the design of integrated magnetic components, modeling for high-power-density power converters, thermal management for power converters, magnetic material applications, and EMI of switching power supply.

Kenkichiro Okamoto received the B.S. degree in electrical and electronic engineering from Yamaguchi University, Yamaguchi, Japan, in 2016. He is currently the M.S. degree with the electrical engineering, Kyushu University, Fukuoka, Japan.

His current research interests include design of magnetic components for dc–dc converters.

Masahito Shoyama (M'93–SM'06) received the B.S. degree in electrical engineering and the Dr.Eng. degree in electrical engineering from Kyushu University, Fukuoka, Japan, in 1981 and 1986, respectively.

He joined the Department of Electronics, Kyushu University as a Research Associate in 1986. He had been an Associate Professor since 1990, and he has been a Professor since 2010. Since 2009, he has been with the Department of Electrical Engineering, Faculty of Information Science and Electrical Engineering, Kyushu University. He has been active in the field of power electronics, especially in the areas of bidirectional converters for dc–ac power systems, high-frequency switching converters for renewable energy sources, power factor correction converters, and electromagnetic compatibility.

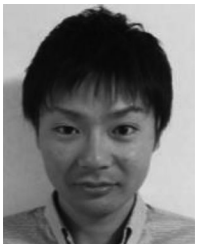

Yuki Ishikura received the M.S. degree electrical and electronic system engineering from Shimane University, Matsue, Japan, in 2012. He is currently working toward the Ph.D. degree with Nagoya University, Nagoya, Japan.

From 2012 to 2014, he was a Circuit Design Engineer with Hitachi, Ltd., Tokyo, Japan. Since 2014, he has been with Murata Manufacturing Co., Ltd., Kyoto, Japan. His research interests include power electronics for dc–dc converters and inverters in renewable energy systems.

Mostafa Noah (S'15) received the M.Sc. degree in electrical engineering from Cairo University, Giza, Egypt, in 2014. He is currently working toward the Ph.D. degree with the Power Electronics Lab, Nagoya University, Nagoya, Japan.

From 2009 to 2015, he was an Electrical Design Engineer with SCG and Dar Al-Handasah. From 2015 to 2017, he was a Research Assistant with the Power Electronics Lab, Shimane University, Matsue, Japan. In Spring 2018, he was with Panasonic, Osaka, Japan, as an intern. His research interests include proposing new magnetic solutions to increase the efficiency and power density of dc–dc converters, including resonant power conversion topologies such as LLC converters.

Masayoshi Yamamoto (M'11) received the M.S. and Ph.D. degree in science and engineering from Yamaguchi University, Yamaguchi, Japan, in 2000 and 2004, respectively.

From 2004 to 2005, he was with Sanken Electric Co., Ltd., Saitama, Japan. From 2006 to 2017, he was with the Interdisciplinary Faculty of Science and Engineering, Shimane University, Matsue, Japan, as an Associate Professor. He is currently a Professor with the Institute of Materials and Systems for Sustainability, Nagoya University, Nagoya, Japan. His research interests include power supply for HEV (boost converter, buck converter, three-phase inverter, digital control), charging system for EV, LED illumination system for a tunnel, EMI of switching power supply, and wireless power transfer.